



TÉCNICO
LISBOA

Simulation of a 3D wall jet cooling of a glass plate oven partition

Rodrigo de Jesus Freire Neno

Thesis to obtain the Master of Science Degree in

Mechanical Engineering

Supervisors: Prof. José Carlos Fernandes Pereira
Dr. Jorge Emanuel Pereira Navalho

Examination Committee

Chairperson: Prof. José Manuel da Silva Chaves Ribeiro Pereira

Supervisor: Dr. Jorge Emanuel Pereira Navalho

Member of the Committee: Prof. Miguel Abreu de Almeida Mendes

June 2021

Força tio!

Acknowledgments

I would like to thank everyone who directly or indirectly made the realization of this thesis possible. Particularly:

To my supervisors. For the opportunity of taking part in this project, for their guidance, transmitted knowledge, and for the availability demonstrated through the realization of the work. Besides my supervisors, I would like to thank Duarte Albuquerque and Beatriz Dias for all the help with the work developed in LASEF and the countless hours via Zoom. I acknowledge also the financial support granted from the European project ECCO.

To my friends. To the friends that accompanied me since the childhood, thanks for all the memories created and the ones will be created in future. To the closest friends that I met on high school which are an inspiration and make my days funnier. To the friendships created during these 5 years which improved my university experience.

To my family, the undoubtedly support in every decisions, specially to my sister. For being a daily inspiration, for the understanding and for being there also as a friend.

Finally, I express my deepest gratitude to my parents, for the trust, values, and dedication passed to me, and without whom this pathway would not have been possible.

Resumo

O processo de revestimento de chapas tem um papel importante na indústria. A evaporação do solvente ocorre convencionamente em fornos por convecção. Neste trabalho, a energia radiativa é usada para aumento da eficiência e para redução da pegada de carbono. O calor radiativo é providenciado por câmaras de combustão e a configuração do sistema considera um vidro dentro do forno para evitar a ignição do solvente. O trabalho é baseado no controlo térmico do vidro para garantir a segurança da operação.

O arrefecimento do vidro por meio de jatos planos de parede permite remover calor a esse meio. Diferentes modelos de turbulência são estudados numericamente em jatos de parede e comparados com correlações disponíveis de transferência de calor para selecção dos mais adequados. Correlações de transferência de calor dos jactos frios são obtidas numericamente para diferentes estratégias de arrefecimento.

O modelo unidimensional (1D) de condução-radiação do vidro é desenvolvido com o método das ordenadas discretas para previsão térmica do meio. O modelo 1D tem em conta correlações obtidas e permite uma análise a diferentes condições de arrefecimento (temperatura, velocidade, ângulo, esquema e outros).

Uma optimização energética baseada num método determinístico oferece as condições ótimas de arrefecimento ao utilizador, respeitando os requerimentos de segurança (máxima temperatura do vidro e gradiente térmico). Por fim, simulações numéricas tridimensionais do forno inteiro são efectuadas para incluir os efeitos que não são considerados no modelo unidimensional e assim providenciar também uma verificação do modelo desenvolvido.

Palavras-chave: arrefecimento de vidros, jactos de parede, radiação-condução, simulações numéricas, optimização energética

Abstract

The coil coating process plays a very relevant role in industry. The conventional process uses convective heat to evaporate the solvent. Instead, in this work radiative heat transfer is used to increase the process efficiency and reduce the carbon footprint. However, the radiative heat was provided by radiative burners and the configuration of the system considered uses a glass plate to avoid ignition of the solvent in the oven. This work is based on the thermal control of the window glass, which aims to guarantee the safety of the operation.

Window cooling by cold wall jets allows to remove heat from the medium. Different turbulence models are used in the numerical calculation of wall jets and are compared against available heat transfer correlations to select the most accurate one. Heat transfer correlations for the cold wall jets are numerically obtained for different cooling schemes.

The one-dimensional (1D) conduction-radiation model with discrete ordinates method is developed to predict the thermal behaviour of the window. The 1D model was developed for fast process characterization, accounts with the heat transfer correlations and provides an analysis of different cooling parameters (temperature, velocity, angle, scheme and others).

An optimization method provides the optimal cooling conditions to respect the safety requirements (maximum window temperature and thermal gradient). Finally, the 3D numerical simulations of the full curing furnace are performed including detailed effects which were not considered on the development of the 1D model.

Keywords: glass plate cooling, wall jets, radiation-conduction, numerical simulation, energy optimization

Contents

Acknowledgments	v
Resumo	vii
Abstract	ix
List of Tables	xiii
List of Figures	xv
Nomenclature	xvii
1 Introduction	1
1.1 Motivation and context	1
1.2 Overview and description	1
1.3 Bibliographic review	3
1.4 Main objectives	6
1.5 Thesis outline	6
2 Non-isothermal wall jet	7
2.1 Physical and mathematical models	7
2.2 $k - \epsilon$ turbulence models	8
2.3 Near wall treatment	9
2.4 Turbulent wall jet	9
2.4.1 Geometry and mesh	9
2.4.2 Validation of turbulence models	10
2.5 Comparison of the redeveloping region of a backward-facing step and a wall jet	14
2.6 Chapter conclusions	16
3 Modeling, simulation, and optimization of glass window	17
3.1 1D window model	18
3.1.1 Energy balance	18
3.1.2 Radiative transfer	19
3.1.3 Convective heat transfer correlations	26
3.1.4 Verification	30
3.2 Results	33
3.2.1 Reference case	33

3.2.2	Effect of spatial, angular and spectral discretisation	35
3.2.3	Effect of window thickness	36
3.2.4	Effect of window thermal conductivity	37
3.2.5	Effect of window radiative properties	37
3.2.6	Effect of surrounding surfaces	38
3.2.7	Effect of cooling gas temperature and velocity	39
3.2.8	Effect of cooling strategy	41
3.2.9	Effect of burner's advective output in cooling	43
3.2.10	Effect of cooling gas injection angle	44
3.3	Energetic optimization	45
3.3.1	Objective function	45
3.3.2	Optimized variables and constraints	47
3.3.3	Results	47
3.4	Chapter conclusions	49
4	3D numerical simulations of the curing oven	51
4.1	Geometrical and modeling details	51
4.1.1	Operating and boundary conditions	53
4.2	Glass thermal analysis	53
4.2.1	Without cooling	53
4.2.2	Cooling inside COS	54
4.2.3	Cooling inside RBS	55
4.2.4	Combined cooling	57
4.3	Energy balances	59
4.3.1	Relevance of wall heat losses	60
4.4	Comparison between the 3D furnace and 1D window model results	61
4.5	Chapter conclusions	61
5	Conclusions	63
5.1	Achievements	64
5.2	Future work	64
	References	65

List of Tables

3.1	Coefficients for heat transfer correlation.	29
3.2	Comparison of average window temperature and absorbed power between 1D model developed and 2D model in ANSYS Fluent for two window thicknesses.	33
3.3	Input parameters for reference case.	34
3.4	Relevance of spatial discretization on window model results and simulation performance: average window temperature and simulation time.	35
3.5	Relevance of DOM angular discretisation on window model results and simulation performance: average window temperature and simulation time.	35
3.6	Relevance of radiative properties spectral discretisation on window model results and simulation performance: average window temperature and simulation time.	36
3.7	Influence of coil temperature on window average temperature.	39
3.8	Influence of burner's radiative efficiency on burner surface temperature and average window temperature.	39
3.9	Average window temperature as function of type cooling.	41
3.10	Window cooling optimization results.	49
4.1	Effect of furnace insulation wall thickness (mineral wall) on the furnace heat losses, furnace walls, and RBS (average fluid).	60
4.2	Comparison of average window temperature between 3D models and 1D model.	61

List of Figures

1.1	3D model of a radiative curing furnace.	2
1.2	Representation of different cooling schemes in a top view: (a) Scheme A; (b) Scheme B; and (c) Scheme C. Red/black arrows indicate cooling direction from above/below the window.	3
1.3	Wall jet nomenclature and representation, extracted from Reference [20].	4
2.1	Mesh geometric features: (a) low-Re mesh; (b) Detailed view under wall jet inlet for low-Re mesh; and (c) Detailed view under wall jet inlet without refinement.	10
2.2	Skin friction coefficient along x for different $k - \epsilon$ turbulence models with wall functions.	11
2.3	Boundary layer growth along x for different $k - \epsilon$ turbulence models with wall functions.	11
2.4	Nusselt number along x for different $k - \epsilon$ turbulence models.	12
2.5	Results for Low-Re modeling simulations along x : (a) skin friction coefficient; (b) growth rate; (c) velocity decay; and (d) Nusselt number.	13
2.6	Results for simulations considering $k - \omega$ SST turbulence model with different meshes: (a) skin friction coefficient profile along x ; and (b) velocity decay along x	14
2.7	Numerical error for different meshes associated to average Nusselt number.	14
2.8	2D velocity contour for numerical simulation with backward-facing step.	15
2.9	Dimensionless velocity profile in y for different turbulence models: (a) SA ; and (b) $k - \omega$ SST.	15
3.1	Schematic representation of curing furnace in a plane perpendicular to the coil.	18
3.2	Flow chart of coupling between energy and RTE equation.	19
3.3	Schematic representation - Intensity radiation.	20
3.4	Plank distribution - Emitted radiation as function of wavelength and temperature (adapted from Reference [53]).	21
3.5	Schematic representation - Intensity radiation on boundary $x = L$	23
3.6	Flow chart of model developed.	25
3.7	Burner's surface temperature with iterations.	26
3.8	Schematic representation - Impinging jet against the window.	26
3.9	RBS geometric model of half battery of burners without the window.	28
3.10	Numerical error associated to wall jet cooling inside RBS.	28

3.11 Numerical average heat transfer correlations for different cooling schemes inside RBS. . .	30
3.12 1D window model validation.	31
3.13 1D window model validation for different emissivities.	32
3.14 Comparison of nondimensional temperature profiles between current model and ANSYS Fluent.	33
3.15 Local divergence of radiative heat flux inside the window.	34
3.16 Window temperature (a) and absorbed power (b) with variable thickness.	36
3.17 Temperature profile for materials with different thermal conductivity.	37
3.18 Temperature profile for material with different radiative properties.	38
3.19 2D contour plot of window temperature dependent of cooling gas injection velocity and temperature.	40
3.20 Dimensionless temperature profiles for cases with cooling inside RBS (a), COS (b), and RBS and COS (c).	41
3.21 Local heat transfer coefficient at the window top surface (window-RBS interface) for dif- ferent cooling schemes: (a) Scheme A; (b) Scheme B; and (c) Scheme C.	42
3.22 2D window temperature for nominal operating condition and different cooling schemes: (a) Scheme A; (b) Scheme B; and (c) Scheme C.	43
3.23 Nusselt number correlation for nominal power and 13% nominal power.	44
3.24 Schematic representation of cooling gas injection angle (β).	44
3.25 Local convection coefficient for numerical simulations with a different angle of injection. . .	45
3.26 Schematic representation of HX situations in both sections.	46
4.1 3D model of the full curing furnace.	52
4.2 2D contour on top surface of the window for the situation without cooling for: (a) incident radiation; and (b) temperature.	54
4.3 Velocity streamlines for recirculation flow with cooling strategy C.	54
4.4 Window temperature distribution for recirculation flow with cooling strategy C.	55
4.5 Temperature contour for different cooling schemes inside RBS: (a) One-sided - Cooling scheme A; and (b) Alternated - Cooling scheme C.	55
4.6 2D contour plot in a longitudinal plane for two different situations: (a) without alignment; and (b) with alignment.	56
4.7 Window longitudinal temperature profile for different cooling gas mass flow rates.	57
4.8 Window temperature distribution with combined cooling.	58
4.9 Streamlines with origin at cooling; (a) Iso-view; and (b) XY view.	58
4.10 Streamlines of velocity (left) and temperature (right) at two different transversal cross- sections: (a) $x=256$ mm; and (b) $x=456$ mm.	59

Nomenclature

Greek symbols

α	Absorptivity [-].
β	Cooling gas injection angle [°].
Δ	Difference between calculated and reference radiative heat flux [W/m ²].
ϵ	Emissivity [-].
κ	Absorption coefficient [m ⁻¹].
κ_t	Thermal conductivity [W/m · K].
λ	Wavelength [μ m].
μ	Direction cosines [-].
ρ	Density [kg/m ³]; and Reflectivity [-].
σ	Stefan-Boltzmann constant [$5.67 \times 10^{-8} \text{ W} \cdot \text{m}^{-2} \cdot \text{K}^{-4}$].
σ_s	Scattering coefficient [m ⁻¹].
τ	Transmissivity [-].
τ_L	Optical coordinate [-].
θ	Non-dimensional temperature [-].
ν	Kinematic viscosity [m ² /s].

Roman symbols

A_{bur}	Area of the burner [m ²].
A_r	Geometrical parameter of impingement jet [-].
A_w	Area of the window [m ²].
b	Jet height [m].
C_f	Skin friction coefficient [-].

D_h	Hidraulic diameter [m].
E	Emissive power [W/m^2].
e	Internal energy [J].
F	Fraction wavelength band [-].
f	Factor to change burner's surface temperature [-].
G	Irradiation field [W/m^2].
H	Enthalpy [J]; and height of slot-surface [m].
h	Specific enthalpy [J/kg]; and convection coefficient [$\text{W}/\text{m}^2 \cdot \text{K}$].
H_λ	Reflection power [$\text{W}/\text{m}^2 \cdot \mu\text{m}$].
I	Intensity of radiation [$\text{W}/\text{m}^2 \cdot \text{sr}$].
I_b	Blackbody radiation intensity [$\text{W}/\text{m}^2 \cdot \text{sr}$].
J	Radiosity [W/m^2].
L	Thickness of the window [m].
\dot{m}	Mass flow rate [kg/s].
N	Conduction-radiation parameter [-].
n	Index of refraction [-].
Nu	Nusselt number [-].
e	Power [J].
Pr	Prandtl number [-].
Q	Thermal power [W].
q	Heat flux [W/m^2].
q_c	Convective heat flux [W/m^2].
q_r	Radiative heat flux [W/m^2].
Re	Reynolds number [-].
S	Source term [-].
T	Temperature [$^{\circ}\text{C}$ or K].
T^*	Non-dimensional temperature by maximum and minimum [-].
T_∞	Surrounding temperature [$^{\circ}\text{C}$ or K].

T_w	Window temperature [$^{\circ}\text{C}$ or K].
u^+	Non-dimensional velocity based on local cell fluid velocity [-].
u_{τ}	Friction velocity [m/s].
U_j	Jet velocity [m/s].
U_m	Maximum velocity of a profile [m/s].
U_{wall}	Overall heat transfer coefficient of the walls [$\text{W}/\text{m}^2 \cdot \text{K}$].
v	Velocity [m/s].
W	Length of slot nozzle [m].
w	Scattering albedo [-].
w_i	Quadrature weights [-].
y^+	Non-dimensional distance based on local cell fluid velocity [-].
y_m	Boundary layer thickness [m].
Y_{rad}	Fraction radiative power of burner [-].

Acronyms

1D	One-dimensional.
2D	Two-dimensional.
3D	Three-dimensional.
COS	Curing oven section.
DNS	Direct numerical simulation.
DOM	Discrete ordinates method.
GA	Genetic algorithm.
HX	Heat exchanger.
IR	Infrared.
RANS	Reynolds averaged Navier-Stokes.
RBS	Radiant burner section.
RTE	Radiative transfer equation.
SA	Spalart-Allmaras turbulence model.
WF	Wall function.

Subscripts/Superscripts

λ Wavelength.

bur burner.

COS Curing oven section.

in inlet.

out outlet.

RBS Radiant burner section.

Chapter 1

Introduction

This chapter provides an overview of the study by presenting initially the motivation and context of the work (Section 1.1) together with a short overview to describe the focus of the work and the conditions of the case studied (Section 1.2). A bibliographic review on relevant topics is presented (Section 1.3). To conclude the chapter, the main objectives of the work are synthesized (Section 1.4) accompanied by the document organization (Section 1.5).

1.1 Motivation and context

The drying/curing process of a metal strip is a relevant process in the industry. This industrial process emerged on 1930's but had its high increase during the 90s [1]. Coating can have different purposes such as functional or even decorative purposes. The process is based on the application of a pre-painted coating, that enters the oven and the energy is provided to drive the thermochemical process on the metal strip. The energy demand for the drying process is high. The process evolved and nowadays techniques are now focused on the search of new efficient techniques. Recent studies are now focused on a change from a convective convectional oven process to a radiative exchange from infrared (IR) burners [2, 3]. The change allows a higher efficiency of the coating process due to less energy demand because the evaporated solvent is used as fuel for the radiant burners [4]. The current work is devoted to an analysis of a radiative curing oven, in more specific, a glass partition inside the oven. The thermal control and analysis of the radiative participating medium is important to assure that the safety requirements are met.

1.2 Overview and description

The curing furnace for this process is composed by two coupled modules (sections). One section is dedicated to the generation of radiant heating (energy source for coating processing) – radiant burner section (RBS) – and the other section is devoted to the coating drying and curing processes – curing oven section (COS), both identified by the red and blue region in Figure 1.1, respectively.

The RBS is the upper section where the burners are placed on ceiling and provide the necessary radiative energy (red arrows in Figure 1.1) to coil coating on the lower section, where a metal strip is continuously fed.

The two domains are separated by a transparent glass (see purple region in Figure 1.1). The glass window is the medium that makes the separation of the two environments, a crucial element for a proper operation. The window composed by an IR-transmissive material prevents the thermal decomposition of the solvent loaded atmosphere (COS) at high temperatures.

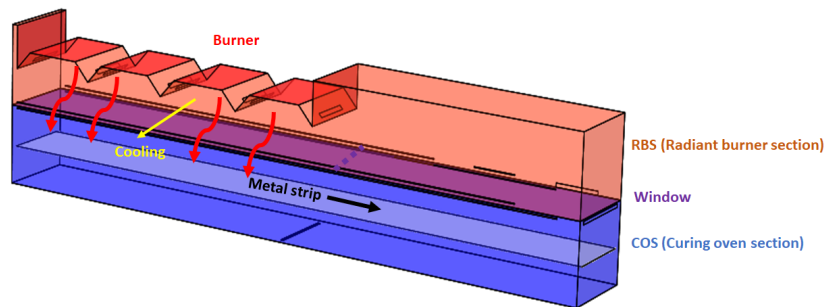


Figure 1.1: 3D model of a radiative curing furnace.

The radiant burners inside RBS are at a very high temperature to provide the necessary radiative energy to evaporate the solvent on the coil. The window is a semi-participating medium to radiation and therefore absorbs part of that radiative energy. The absorption of energy is prejudicial since removes radiative energy for the curing process and also leads to high temperatures inside this medium. The magnitude of the temperature inside the window must be below the critical values of the material to avoid the development of thermally induced mechanical stresses leading to the window structure fatal failure. The current work is focused on the modeling, simulation, analysis, and optimization of the glass oven partition.

A cooling system is a very important strategy used to remove heat from the window and therefore reduce its temperature. The cooling jet is injected parallel to the window by a cooling slot, in a transversely direction to the movement of the coil (see yellow curve in Figure 1.1). The wall jet faces a backward step at the injection and the flow develops until achieves the perpendicular wall at the end of the window. There are different cooling schemes which are possible to install, and are schematically represented in Figure 1.2. The red arrows represent the direction of the cooling injection from above the window (RBS) and the black arrows from underneath the window (COS).

- A - One-sided cooling

The cooling jet is injected from one side on the upper part of the window (RBS) as the red arrows indicate in Figure 1.2. The strategy is coupled with cooling injection on the opposite side on the lower part (COS).

- B - Two-sided cooling

This strategy is based on the injection from both sides, both on upper and lower region of the window. The velocities here are reduced to half to respect the mass flow rate of cooling inserted

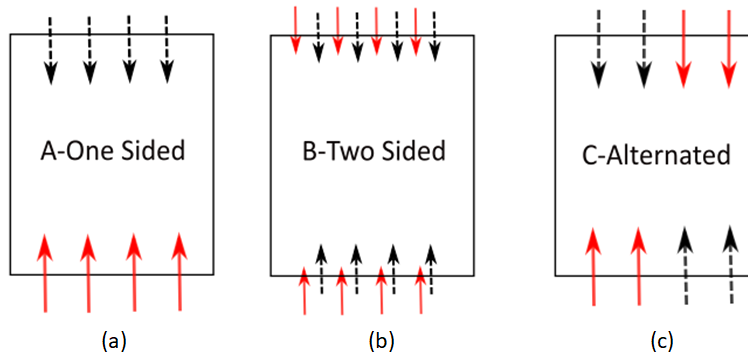


Figure 1.2: Representation of different cooling schemes in a top view: (a) Scheme A; (b) Scheme B; and (c) Scheme C. Red/black arrows indicate cooling direction from above/below the window.

to the system. The arrows are not overlapped just for a observation point of view but the cooling from above and underneath the window are completely aligned.

- C - Alternated cooling

The mechanism is similar to cooling scheme A but the difference is that the side of injection is variable with the window length. The variation happens also inside COS to an alignment as the arrows indicate.

The cooling system is enabled on both sections (RBS and COS) due to recirculation systems. An extraction port removes the flow from the environments, passes the fluid through an outside heat exchanger (HX) and then the cold flow is inserted again into the system from above and underneath the window. There are two different HX due to the different environments (RBS and COS). The energetic optimization of this work provides the optimal operating condition (reduced energy cost of the HX) by manipulating the cooling gas velocity and temperature, respecting the safety requirements of the glass partition (maximum temperature and gradient inside the window). The optimization also dictates which is the most suitable cooling scheme.

1.3 Bibliographic review

The following bibliographic review highlights the main topics of the study but more theoretical content is introduced along the work.

One of the topics of this study is the radiation heat transfer in participating media. Viskanta and Grosh [5] obtained a solution for the one-dimensional study using a transformation of the integro-differential equation into a non-linear integral equation solved iteratively. The studies on this topic emerged, specially in terms of processing time and convergence. Those recent models have an agreement with the initial studies in terms of accuracy but offer better solutions in terms of computational efficiency [6, 7]. The window model is developed according with an iterative process between energy and radiative transfer equation and the solution method to angular discretisation of the radiation intensity used in this work

is the discrete ordinates method (DOM). The first DOM was proposed by Chandrasekhar [8] and the method had other objectives. The method was adapted by Thynell [9] and the study is now generally used in heat transfer problems. The DOM is very adequate since considers the absorption of radiation inside a medium, in opposite to other radiation models which are only focused on the radiative exchange between surfaces. The DOM is suitable for similar cases with high temperatures as benchmarks demonstrate [10].

The participating medium (window) is affected not just by the conduction and radiation, but also by convection on the boundaries. The heat transfer implied by the wall cold jet above and underneath the window is one of the topics highlighted during the work. A wall jet is defined as an injection of high-momentum fluid into a thin layer along a wall (see Figure 1.3). This type of cooling is very efficient and suitable to the current industrial process. The wall jet cooling has other industrial applications such as flaps of an airfoil [11], gas turbine blades and combustion chamber walls exposed to gases. The wall jet cooling can act as "curtain" to the window and remove heat from the surface.

Wall jets started to be studied by Glauert [12], in mid 1950s, by deriving an analytical solution for laminar and turbulent jets. A self-similar solution was found for laminar wall jet and the study provided a good basis for the following theoretical, experimental and numerical studies on the physics of wall jets. Launder and Rodi [13] made a review of those studies up to 1983, not only summarizing but including the Reynolds average turbulence modeling required, where wall jets are treated as two different layers, inner and outer layer.

The inner wall resembles a boundary layer from the wall to y_m , which U_m is the velocity at the outer edge and y_m , the boundary layer thickness. The outer layer, from y_m to the outer edge of the flow, represents half of a free jet. The several experimental studies showed that U_m and $y_{1/2}$ can be used to collapse the velocity profile in the outer layer, as is the case for free jets [14, 15]. In the inner layer of the wall jet, the one seventh power law was initially used to describe the turbulent boundary layer.

The studies demonstrated that there are differences between inner and outer layer, and the boundary layer and free shear flow studies, respectively. Those differences are due to the interaction between those two layers, which creates modifications on both. George [16] developed a theoretical study where demonstrates that the profiles have a self-similar solution by an adequate inner and outer scaling. The friction velocity, u_τ , and the length scale, $\frac{\nu}{u_\tau}$, are the proper velocity and length scale, respectively, for the inner layer. U_m and $y_{1/2}$ are the velocity and length scales used for outer layer. The theoretical study was corroborated and validated with other experimental studies [17–19].

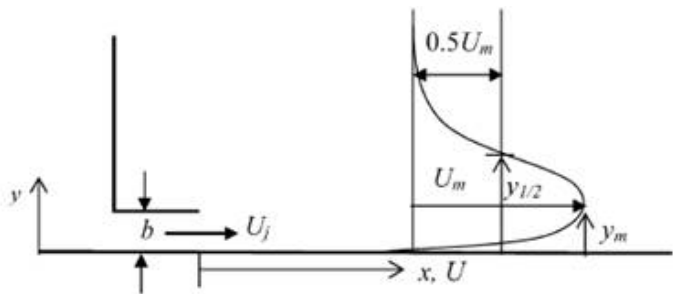


Figure 1.3: Wall jet nomenclature and representation, extracted from Reference [20].

The heat transfer studies on this topic have received much lower attention than the isothermal case. Dacos [21] measured experimentally, temperature and heat fluxes for plane and curved wall jets with isothermal conditions and AbdulNour *et al.* [22] with an experimental study, measured the convective heat transfer coefficients up to $x/b = 20$. Naqavi [23] completed a recent direct numerical simulation (DNS) study focused on the heat transfer of a wall jet up to $x/b = 40$. Other initial experimental studies show that at fully developed downstream locations, a correlation can be applied:

$$Nu = C \times Re^{0.8} \times \left(\frac{x}{b}\right)^{-0.6} \quad (1.1)$$

where C is a empirical coefficient varying from 0.071 [24] to 0.115 [25].

Optimization techniques were developed to improve typical trial and error techniques. They are based as well in iterative processes but differ since optimization has a systematic adjustment on each iteration based on evaluation of certain parameters. The trial-and-error strategy is based only in designer's intuition and experience to improve the process, while optimization changes the search based on sensitivity information and numerical algorithms which aim to maximize the improvement between successive iterations. In consequence, trial and error strategies usually have a higher computation effort and can result in results not as exact as from optimization. The objective of the problem could be obtained in a trial and error strategy by constant evaluation of the objective function for different cooling conditions to find the minimum. This trial and error strategy can be misleading in some cases due to discretisation and could be quite time consuming.

Optimization methods differ in how the objective function is minimized, and they can be classified as deterministic or meta-heuristic [26]. Deterministic methods focus the search and the algorithm by changing the domain at each step based on the local topography of objective function. In meta-heuristic algorithms, the domain is selected from a large set of candidate solutions generated by a random process. Meta-heuristic approaches include simulated annealing, genetic algorithms, neural networks and tabu search.

Two different solver methods were explored: interior-point and genetic algorithm. The interior-point method also referred to as barrier methods are a certain class of algorithms that solve linear and non-linear convex optimization problems. The interior-point method is part of deterministic optimisation technique. This method was initially developed by Narendra Karmarkar in 1984 [27], when a fast polynomial-time method was announced for linear programming. Afterwards, connections were established between his method and classical methods, and the exploitation on interior methods suffered a huge expansion with more than 2000 papers and reports published during the 90's, where the researchers focused on the improvement of both theory and practice of constrained problem [28–30]. The deterministic methods suffers from disadvantages such as the detection of infesiability. Fortunately, new models were developed with quite similar computational effort [31]. The other disadvantage is that the optimization can suffer from a lack of accuracy by finding local minimums. In such cases, the minimum obtained could be deceitful since is based on an initial point and the minimum can offer a local solution instead of a global. The situation can be overpassed by the coupling with other algorithms such as multi-start and global

search. The first algorithm starts with different initial points to guarantee more reliability and the second is based on the same idea but uses scatter-search mechanism to generate the starting points [32, 33].

Genetic algorithms (GA) is another algorithm which is explored. The algorithm is based on the principle of biological evolution, inspired by Darwin's theory about the survival of the most adequate member. The idea was developed and introduced by John Holland and his collaborators in the 1960s and 1970s [34], where the result of their work was the basis of a new area of interest and research with applications that go much wider than the original GA. The population (initial random points) is generated and according with the fitness of the individuals and the constraints, the next generations evolve to bring the optimal solution of the problem. The generation, crossover and mutation rules are applied to the search of the most adequate member. The GA considers the entire region of interest but suffers from disadvantages when the population is non-linearly constrained. The most common technique is apply a penalty function [35, 36].

1.4 Main objectives

The work is focused on the analysis of a radiative curing furnace, and in specific, the modeling, simulation, analysis, and optimization of the glass window thermal performance between RBS and COS.

The first objective of the work is the selection of adequate turbulence models for simulation of turbulent wall jets. This analysis is of extreme importance to understand the reliability of the models used on the numerical simulations of cold wall jets. A one-dimensional window model is developed and simulated to offer prediction of the thermal behaviour under certain operating conditions. The accomplishment of this objective is important to answer questions such as the proper functioning of the system and understand the influence of certain design and operating parameters. In addition, the current work develops an optimization procedure to provide the optimal conditions. The other main objective of the present study is then, optimise the layout and operating cooling conditions to achieve a stable and safe operation of the window. The final objective is achieved with numerical simulations of the full radiative curing furnace which verify the work performed.

1.5 Thesis outline

The work is divided in 5 chapters. The initial chapter is introductory to the subject and work performed. The overall modeling employed is presented together with the turbulence model performance for wall jet cooling in Chapter 2. The optimisation technique and the 1D model of the window developed are described in Chapter 3. The complete 3D numerical simulations of the full radiative furnace are analysed in Chapter 4 and the final conclusions of the work are listed in Chapter 5.

Chapter 2

Non-isothermal wall jet

This section intends to perform a validation study of the numerical error associated to simulation of wall jets. An initial bibliographic review regarding wall jets is already presented on the previous chapter (Section 1.3) and this chapter intends to present the physical and mathematical models, the turbulence models which will be analyzed and the near wall treatment necessary (Section 2.1, 2.2, and 2.3). The geometry, mesh and simulation details are presented for the case of the turbulent wall jet. The results are discussed considering two different approaches (Section 2.4). The situation with the wall jet facing a backward step at the entrance is also herein analyzed (Section 2.5) and consequently the conclusions drawn (Section 2.6).

2.1 Physical and mathematical models

A flow field is characterized by mass, momentum, and total energy balances described by the continuity equation, the Navier-Stokes equations, and the total energy equation, respectively. The solution to the mathematical model equations provides the velocity field (v), pressure (p), and temperature (T) of the fluid in the modeled domain.

For newtonian fluids, the viscous stress is proportional to the deviatoric stress tensor:

$$\tau = \mu(\nabla v + \nabla v^T) - \frac{2}{3}\mu I(\nabla \cdot v) \quad (2.1)$$

The flow can be classified as incompressible if the density variations are very small, if $\Delta\rho/\rho \ll 1$. This is true for liquids (unless there are significant temperature variations) and gases under moderate pressure and temperature variations. If we can neglect the heating due to viscous dissipation (so called viscous heating) and assume that the fluid is newtonian, the continuity, Navier-Stokes, and total energy equations can be simplified to:

$$\frac{\partial \rho}{\partial t} + \nabla \cdot (\rho v) = 0 \quad (2.2)$$

$$\frac{\partial(\rho v)}{\partial t} + \rho v \cdot \nabla(v) = -\nabla p + \nabla \cdot \tau + F \quad (2.3)$$

$$\rho C_p \frac{\partial T}{\partial t} + \rho C_p v \cdot \nabla T = \nabla \cdot (k_t \nabla T) + S_e \quad (2.4)$$

As it can be seen, the energy equation has been rewritten as a temperature equation, which is much more convenient to work with. The temperature equation is for incompressible flows completely decoupled from the Navier-Stokes equations, unless the viscosity depends on the temperature which is the case.

The numerical simulations were performed in a commercial software (ANSYS Fluent) with mass, momentum and energy equations for steady flow in a time average formulation (RANS):

$$\frac{\partial(\rho v_i)}{\partial x_i} = 0 \quad (2.5)$$

$$\frac{\partial(\rho v_i v_j)}{\partial x_j} = \frac{\partial p}{\partial x_i} + \frac{\partial}{\partial x_j} \left[\mu \left(\frac{\partial v_i}{\partial x_j} + \frac{\partial v_j}{\partial x_i} - \frac{2}{3} \delta_{ij} \frac{\partial v_i}{\partial x_j} \right) \right] + \frac{\partial}{\partial x_j} (-\overline{\rho v_i' v_j'}) \quad (2.6)$$

$$\frac{\partial(\rho C_p v_i T)}{\partial x_i} = - \frac{\partial}{\partial x_i} (k_t \frac{\partial T}{\partial x_i}) + S_e \quad (2.7)$$

The Reynolds stresses ($-\overline{\rho u_i' u_j'}$) must be modeled according with the turbulence model. The transport equation for a scalar variable:

$$\overline{\rho u_j} \frac{\partial \bar{\phi}}{\partial x_j} - \frac{\partial}{\partial x_j} \left[\Gamma_{\phi,eff} \frac{\partial \bar{\phi}}{\partial x_j} \right] = S_\phi \quad (2.8)$$

where ϕ represents the species mass fractions as well the variables of turbulence models, $\Gamma_{\phi,eff}$ the effective diffusion coefficient, and S the source term of the equation.

2.2 $k - \epsilon$ turbulence models

The following turbulence models within Fluent were considered for comparison and analysis:

- Standard $k - \epsilon$ model with standard wall function (WF) [37];
- Standard $k - \epsilon$ model with scalable WF [38];
- Realizable $k - \epsilon$ model with standard WF [39]; and
- Standard $k - \epsilon$ model with non-equilibrium WF [40].

and the low-Reynolds models:

- $k - \epsilon$ low Reynolds Yang Shih [41];
- $k - \epsilon$ low Reynolds AKN [42];
- $k - \omega$ SST (Menter) [43]; and
- Spalart-Allmaras (SA) [44].

2.3 Near wall treatment

The no-slip boundary condition of the bottom wall influences the development of the turbulent boundary layer and provides steeper gradients of velocity near the wall. The modeling is influenced by its growth. The boundary layer region has been studied and subdivided into three different regions: the laminar sublayer ($y^+ < 5$), buffer region ($5 < y^+ < 20$), and the log-law region ($20 < y^+ < 0.1\delta$) which typically a few percent of the boundary layer thickness but it depends of the pressure gradient.

A mesh with the first cells placed inside the laminar sublayer is referred as low-Re modeling and the mesh should be refined enough as the first cell be at $y^+ < 1$. Modeling a mesh with the first cell in the buffer region is not advisable since the behaviour is not defined as the viscous sublayer ($u^+ = y^+$) and as the log-law region ($u^+ = 1/k \times \ln(y^+) + C^+$). For meshes with the first cell at $y^+ > 20$, wall function theory can be applied. The wall function offers a good prediction inside the boundary layer without the need of a fine mesh at the surface of the wall, reducing the computational effort of a simulation.

2.4 Turbulent wall jet

The wall jet enters the domain with a certain velocity and develops along x , see Figure 1.3.

Reynolds number (ratio of inertial forces to viscous forces) is defined, specifically for wall jet, as:

$$Re_j = \frac{U_j \times b}{\nu} \quad (2.9)$$

where b (jet height) is defined as the characteristic length.

The transition between different states of flow is not directly defined by Reynolds number since its characteristic length(jet height) and velocity (inlet velocity) are fixed. This means, a flow can be at laminar state with a Reynolds number equal to 4000 while other jet with Reynolds number equal to 2000 is at turbulent, fully developed state. The region analysed also dictates the state. The flow with Reynolds number equal to 4000 is analyzed almost at the inlet while the other one is analyzed after the development. Nevertheless, the Reynolds number has a high impact on the transition process. An experimental study [45] demonstrated when the Reynolds number is higher than 2000, the wall jet velocity profile changes almost directly from a uniform velocity distribution to a turbulent wall jet distribution in the developed region. Experimental values [22] for the case studied ($Re_j = 7500$) also show that this region of development is very reduced (up to $x/b = 7$).

2.4.1 Geometry and mesh

The DNS study [23] was used to validate the models considered and simulate wall jets. The jet enters the domain at $Re_j = 7500$ from an inlet with height equal to 20 mm. The jet inlet temperature is constant and equal to 22°C. The jet develops streamwise along a no-slip isothermal wall at 44°C. The computational domain has the dimensions of $50b$ and $40b$ in x and y directions, respectively. The remain normal wall ($x = 0$) at the injection provides the jet entrainment with a uniform flow at $0.06 U_j$. The upper boundary

($y = 40b$) has a free slip boundary condition.

The mesh varies in x and y direction with a ratio since the refinement near the injection and near the bottom surface is more relevant to simulate the behaviour of the jet (see Figure 2.1(a)). The injection of the wall jet is identified by the black circle at left bottom of the domain.

Low-Re modeling strategy is based on the modeling of the low Reynolds turbulent region from the viscous sublayer to the log-law. Consequently, the reduction of the mesh size near the wall is mandatory. For current simulations, the first cell stays inside $y^+ < 1$ and a considerable number of cells inside the viscous sub-layer (see Figure 2.1(b)). For $k - \epsilon$ models with wall functions, a common mesh comprising 50×55 points was considered. The mesh does not have a refinement near the wall, only with enough mesh resolution inside the jet height (10 divisions). The difference is evident by comparison of Figures 2.1(b) and (c).

The simulations were iterated until the scaled residuals were below 10^{-6} .

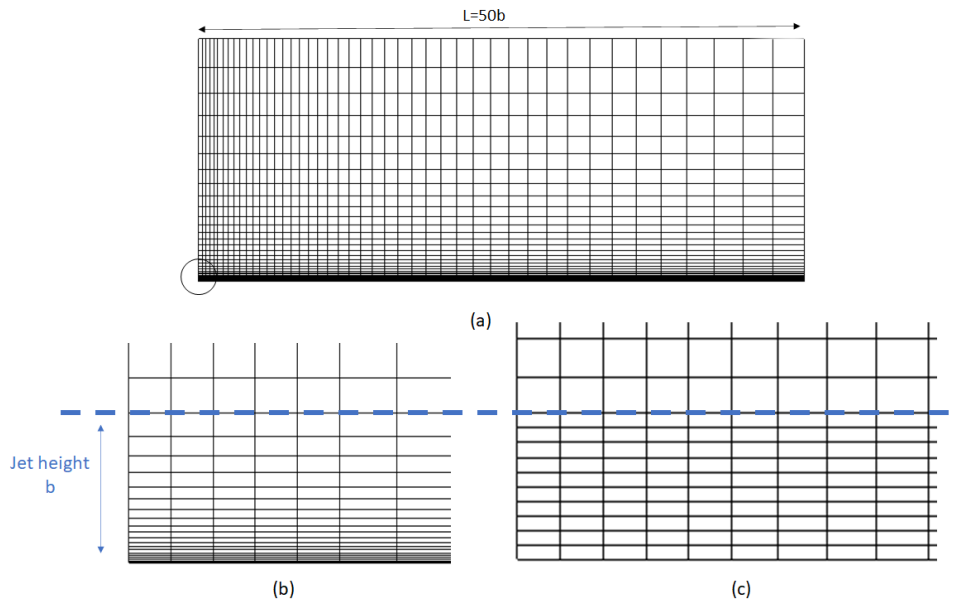


Figure 2.1: Mesh geometric features: (a) low-Re mesh; (b) Detailed view under wall jet inlet for low-Re mesh; and (c) Detailed view under wall jet inlet without refinement.

2.4.2 Validation of turbulence models

The first results are presented by considering the turbulence models with wall functions. Figure 2.2 represents the skin friction coefficient along x for the numerical and DNS simulations [23]. Large differences on the initial region are expected due to the laminar and transitional state of the flow (peak at $x/b \approx 15$). The transitional boundary layer flow developed by the wall jet can be well predicted leaving the present wall functions and high turbulent Reynolds number models. Consequently, the transitional region - denoted by the peak in skin friction coefficient is at different locations. However, the simulations with the different turbulence models present similar results to DNS in the fully turbulent region, after $x/b > 20$.

Figure 2.3 shows the growth rate of the flow along x , represented by the streamwise jet half width

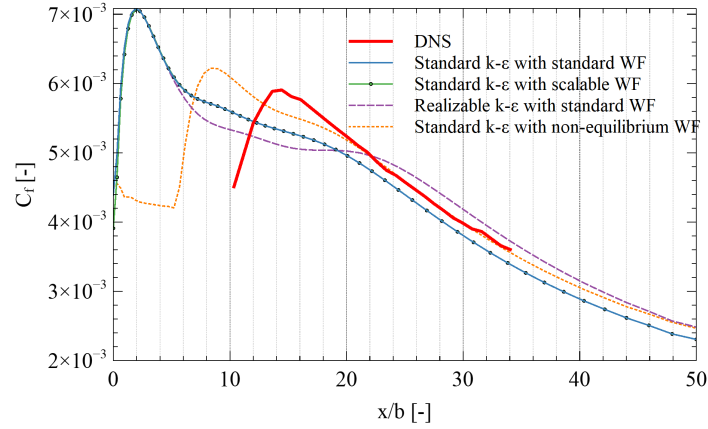


Figure 2.2: Skin friction coefficient along x for different $k - \epsilon$ turbulence models with wall functions.

($y_{1/2}$). Figure 2.3 demonstrates that the results obtained with numerical simulations have an error when compared with DNS simulation and with the linear relationship proposed by Abrahamsson *et al.* [18]: $0.0732x/b + 0.332$. The derivative of growth rate (slope in Figure 2.3) was evaluated and the error associated to numerical simulations varies from 17.7% to 24.7% according with different models.

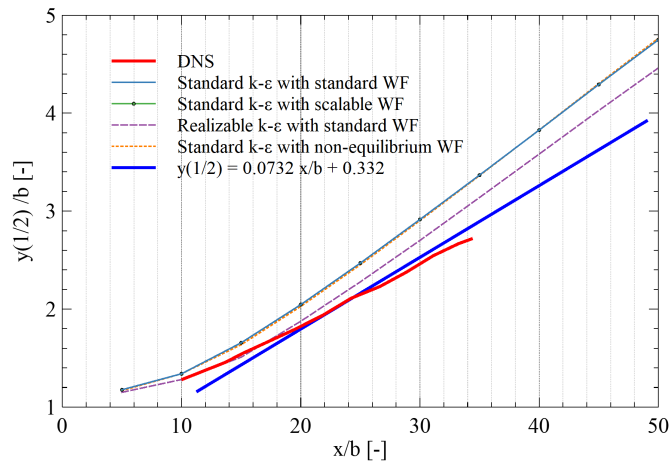


Figure 2.3: Boundary layer growth along x for different $k - \epsilon$ turbulence models with wall functions.

George [16] demonstrated that the linear relationship is not a complete correct relationship since has a slight dependence on the derivative. For the specific conditions of the problem studied (Reynolds and region considered) that dependence is not observed in Figure 2.3. Figure 2.3 shows that realizable $k - \epsilon$ model (pink dashed line) registers values closer to DNS results. However, the line is almost parallel to the ones registered with the other models (same slope) which does not prove more accuracy. The model is predicting the same growth rate after the transitional region.

The Nusselt number is a dimensionless parameter commonly used in convection heat transfer studies. The graph of Figure 2.4 is in logarithmic scale and presents $NuRe^{-0.8}$ in the y scale. The scale allows a better visualization of results by comparison of the empirical coefficient C (Equation (1.1)). The values obtained with the turbulence models slight overpredict the heat transfer on the turbulent region ($x/b > 20$) but are closer to experimental values measured.

The accuracy of the turbulence models depends on the capability to predict the behaviour near the wall, inside the boundary layer. Wall functions on turbulence models are valid where $y^+ > 20$. The dimensionless parameter was evaluated in the simulations and the values are not within the range of validation, becoming lower than 20 at middle of the domain and equal to 15 at the end of the domain. Simulations were performed by increasing the first cell size but that originated too low resolution inside the remain jet structure.

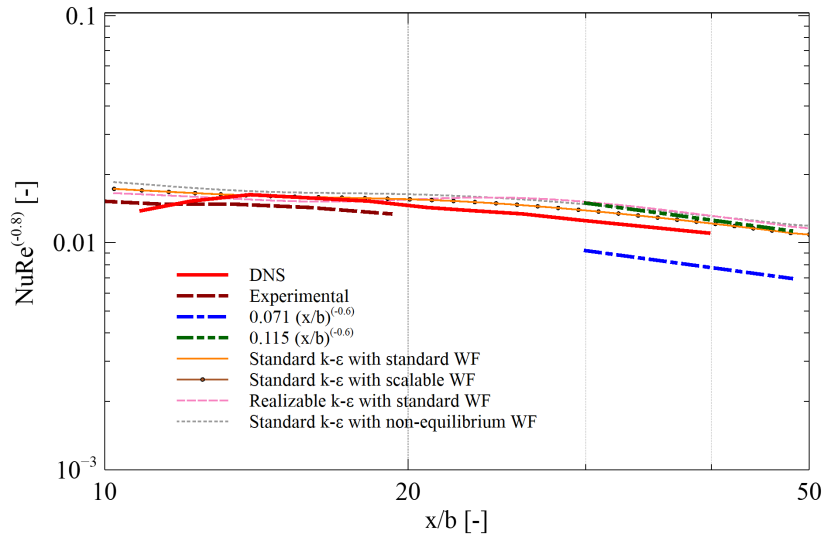


Figure 2.4: Nusselt number along x for different $k - \epsilon$ turbulence models.

The low-Re modeling with the adequate turbulence models was then analysed. Figure 2.5 compare the results obtained with the different low-Re turbulence models with DNS [23], by representing: the skin friction coefficient (Figure 2.5(a)) associated to shear stresses and friction velocity (u_τ) along x ; the growth rate of boundary layer ($y_{1/2}$) and the velocity decay (U_m) along x in Figures 2.5(b) and (c), respectively; and the Nusselt number representing the heat transfer along the wall in Figure 2.5(d).

Both low-Re $k - \epsilon$ models provide similar predictions. The models predict the transitional behaviour as can be observed by the peak at $x/b \approx 16$ in Figure 2.5(a). Despite the consistent response to this behaviour, the model shows lack of accuracy on the prediction of flow behaviour. This lack of accuracy can be observed by the boundary layer growth rate with an error of around 28% in Figure 2.5(b), predicting an higher velocity decay. Both models also over predict Nusselt number as can be observed in Figure 2.5(d). The results obtained with $k - \omega$ SST model do not simulate the transitional region but assume fully turbulent from the beginning. Despite the lack of accuracy on the initial region, the results show consistent values in comparison with the studies already performed. The agreement is specifically evident in Figure 2.5(b) - marked blue line - with an error associated of 6.8%. The results obtained with SA model demonstrate that the model is adequate for low-Re wall jet modeling (orange line) as already demonstrated in a similar study [46]. This one equation model was especially developed for aeronautics and wall-bounded flows and provides high accuracy as can be observed by the graphs. This accuracy is evident on the evaluation of the growth rate of boundary layer, where the slope shows an error of only 1%. The low-Re modeling with adequate turbulence models provides more accurate

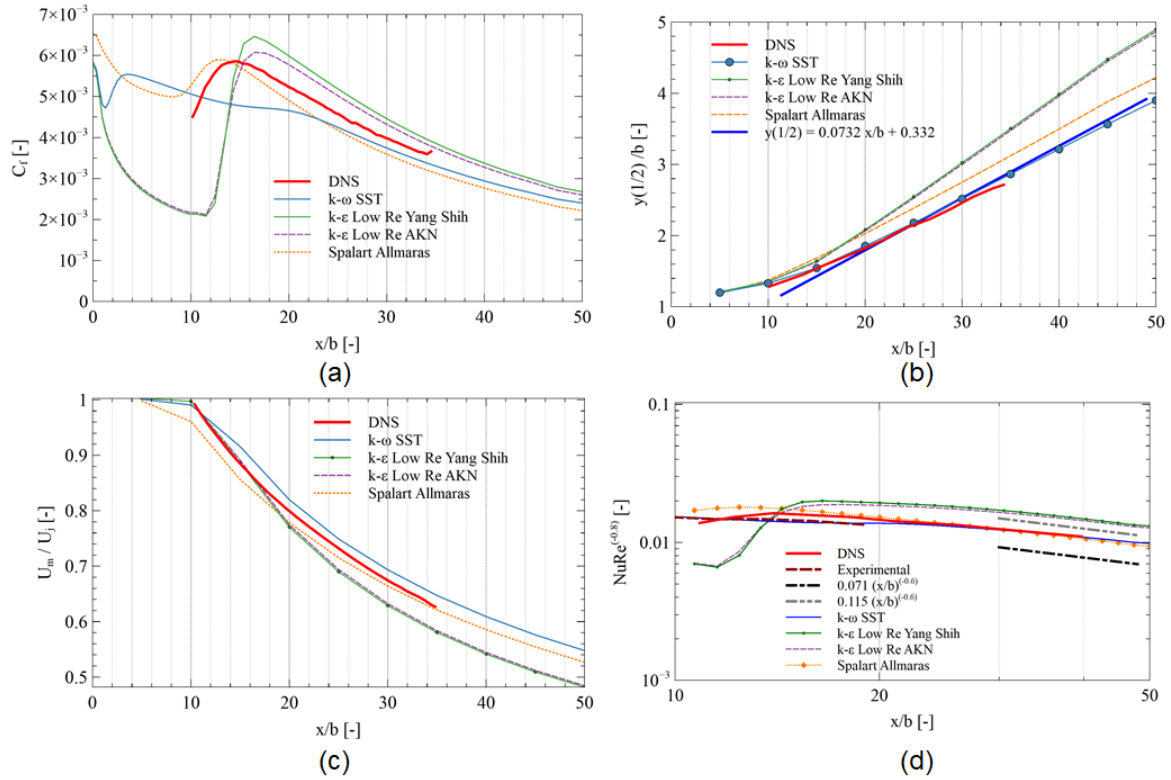


Figure 2.5: Results for Low-Re modeling simulations along x : (a) skin friction coefficient; (b) growth rate; (c) velocity decay; and (d) Nusselt number.

results for the case studied. A similar recent study with flow over a smooth flat plate demonstrated also that difference by low-Re modeling [47].

Previous numerical simulations showed that the model $k - \omega$ SST provided consistent results on the study of wall jets as other studies already compared in impingement jets [48]. Numerical errors are associated to numerical simulations and to dissipate and investigate this aspect, different meshes were considered and inspected.

The mesh considered on the previous section (Figure 2.1(a)) was double refined in both directions and almost no differences are observed in terms of skin friction coefficient and velocity decay (Mesh 4 and 5 in Figure 2.6(a) and (b)). Consequently for this boundary layer, the numerical error is not the main issue but modeling.

Increasing the mesh base size near the wall and considering less points inside the viscous layer results in a different prediction (Mesh 3). The differences are only verified in the transitional region, where coarser meshes without refinement near the wall show large differences. The velocity decay of a fined mesh (brown line in Figure 2.6(b)) is closer to a DNS simulation than the coarser (blue line).

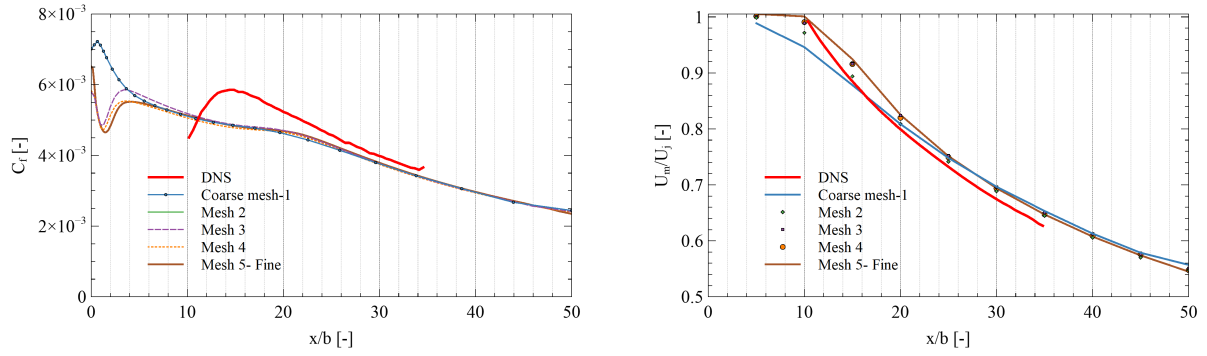


Figure 2.6: Results for simulations considering $k - \omega$ SST turbulence model with different meshes: (a) skin friction coefficient profile along x ; and (b) velocity decay along x .

The average Nusselt number (considering $10 < x/b < 40$) was evaluated and the absolute error for the different meshes is plotted in Figure 2.7. The numerical error for the coarser mesh is 11.3% (left side) while the refined mesh (right side) presents a lower error of 4%. Despite the differences and the highest numerical error inside the initial region, a coarser mesh presents similar results to a refined mesh at a fully turbulent region.

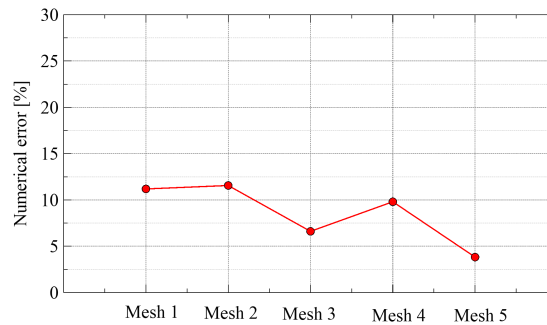


Figure 2.7: Numerical error for different meshes associated to average Nusselt number.

2.5 Comparison of the redeveloping region of a backward-facing step and a wall jet

The case of the jet being injected perfectly aligned with the wall is not applicable for the industrial process analysed in this thesis due to construction constraints. Therefore the jet faces a backward step at the injection. Question arise in what is the influence of the recirculation region of the backward facing step on the flow development, and their comparison with a wall jet flow.

A numerical simulation similar to previous simulations using $k - \omega$ SST and SA turbulence model was performed with a step equal to 3 times the jet height. Figure 2.8 shows velocity contours where the effects previously described such as separation region and attachment can be observed. The location of flow attachment depends on several conditions such as the Reynolds number, aspect ratio between

depth of flow and height of the step, situation of confined or non-confined channel and others. However as other studies demonstrate [49, 50], the wall jet remains with the same behaviour after the attachment.

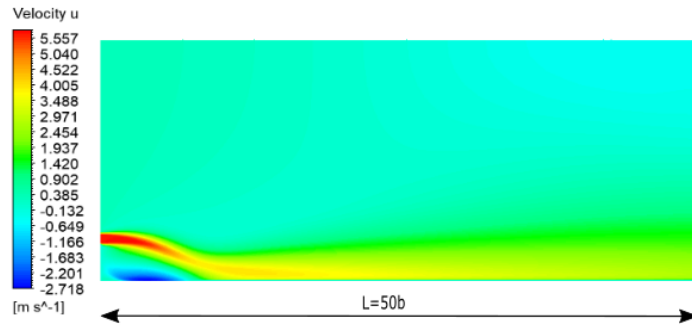


Figure 2.8: 2D velocity contour for numerical simulation with backward-facing step.

The wall jet behaviour is proved by the results observed in Figures 2.9(a) and (b). Figure 2.9 displays the dimensionless velocity profile at two different regions, $x/b = 30$ and $x/b = 45$, for simulations with and without backward-facing step. Figures 2.9(a) and (b) represent numerical simulations with SA model and with $k-\omega$ SST turbulence model, respectively. The graphs show that the velocity profiles are aligned between the two different situations (with or without step) and are very similar to the self-similar situation for fully turbulent region. There are slight differences between the turbulence models as expected since the SA model is based in only one turbulence equation.

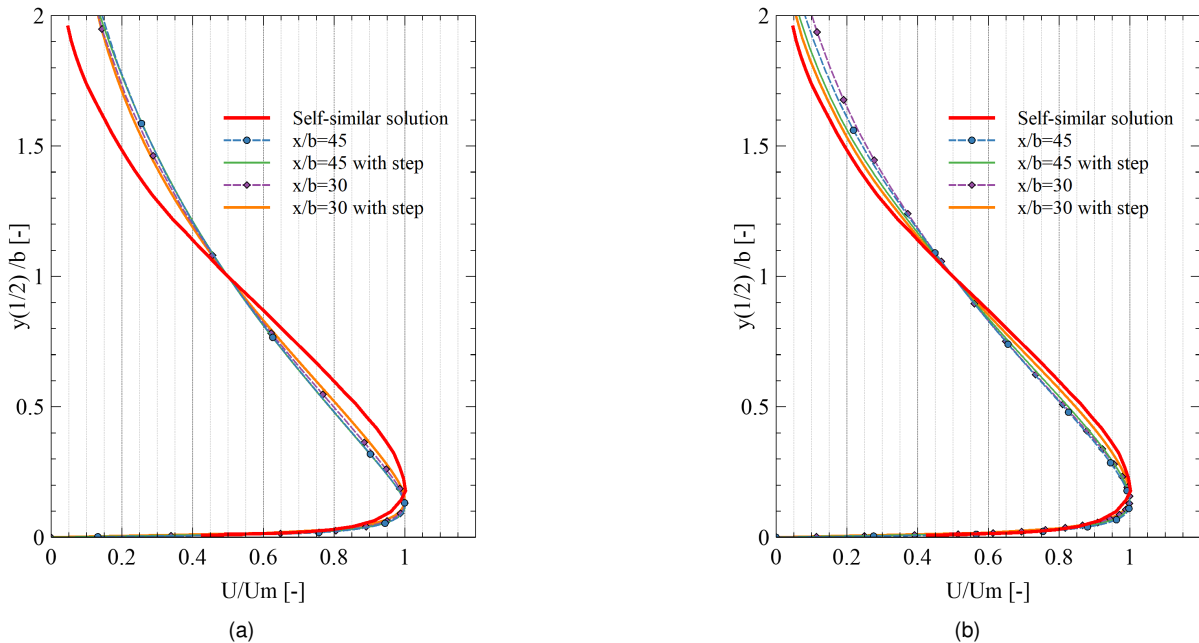


Figure 2.9: Dimensionless velocity profile in y for different turbulence models: (a) SA ; and (b) $k-\omega$ SST.

The results inside the recirculating region and attachment are not focus of interest since the attachment is registered approximately at $x/b = 7$, which represents a small fraction when compared with the region that is going to be future focus of the study, $x/b = 120$ (around 5%).

2.6 Chapter conclusions

Turbulence models for the wall jet case studied show lack of accuracy in transitional regions since these models assume turbulent flow regime almost from the beginning. The lack of accuracy on this region does not become problematic since the region of interest in this thesis is up to $x/b = 120$ and the wall jet faces a backward-facing step at the inlet, that triggers the boundary layer to become turbulent. Different turbulent models with different modeling were investigated, where $k - \omega$ SST and SA models with low-Re modeling proved to have higher accuracy. The grid size demonstrated differences on the transitional region but a coarser mesh proved to have similar results as a refined mesh on the fully turbulent region. The study of a wall jet with a backward-facing step equal to 3 times the jet height demonstrated that after the attachment, the flow behaves as a typical wall jet.

Chapter 3

Modeling, simulation, and optimization of glass window

This chapter intends to demonstrate the methodology used on the optimization procedure of the cooling. The high computational effort of an optimization procedure resorting to 3D numerical simulations of the entire oven is unreasonable, therefore the strategy was based on the development of a more simple case - one-dimensional (1D) model. Numerical simulations associated to wall jets on a reduced geometrical model without the window provided the necessary heat transfer correlations. This information was integrated with the model developed and analysed. The first section covers the development of the model (Section 3.1). The results and the influence of different parameters are further inspected (Section 3.2). The following section describes the optimized variables, the project requirements and the objective function of the optimised technique (Section 3.3). The conclusions are listed in Section 3.4.

3.1 1D window model

This section describes the 1D model developed to predict the thermal behavior of the glass plate - compute the temperature distribution inside the window. A simplified 1D model is considered to reduce the extremely high computational effort of the 3D numerical simulations.

Figure 3.1 represents schematically the situation inside an oven. x is the dimension of study along the thickness of the window, with $x = 0$ at the surface in contact with the COS.

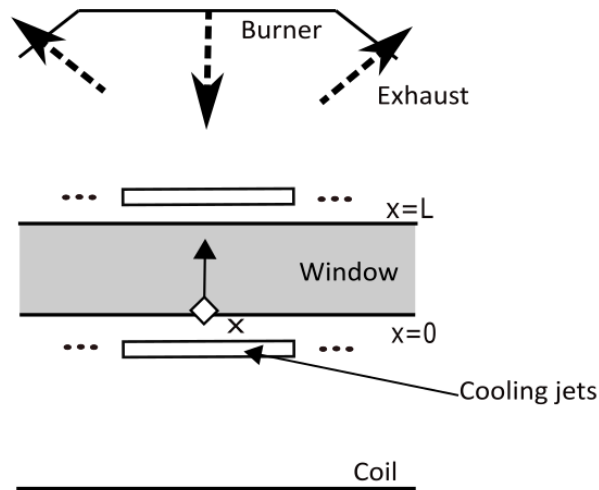


Figure 3.1: Schematic representation of curing furnace in a plane perpendicular to the coil.

3.1.1 Energy balance

The thermal conductivity (k_t) is assumed constant along the thickness (x) since the difference of temperature inside the window for the cases studied will not be significant (reduced window thickness - 2 mm). The energy equation for the solid glass in a steady-state form reads as:

$$k_t \frac{d^2 T}{dx^2} = \frac{dq_r}{dx} \quad (3.1)$$

The divergence of radiative flux is directly related with the radiation intensity inside the medium. The radiation intensity can be computed according with the radiant transfer equation (RTE). The coupling between the two equations (RTE and overall energy balance) is non-linear due to the divergence of radiative flux depending on terms non-linear, such as T^4 . An iterative procedure used on the development of this model is described in the flow chart of Figure 3.2.

The iterative process stops when residual value becomes lower than 10^{-6} .

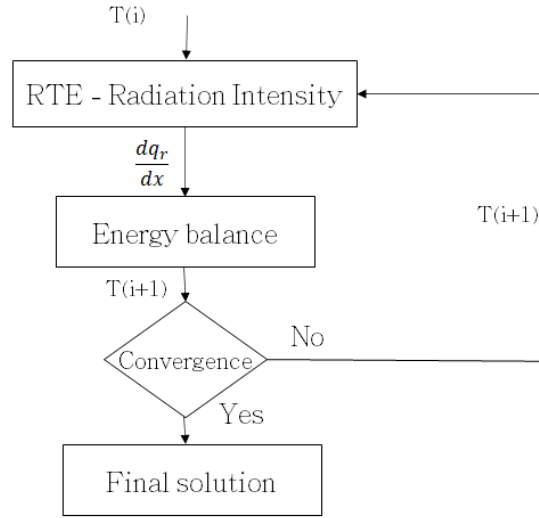


Figure 3.2: Flow chart of coupling between energy and RTE equation.

Equation (3.1) was solved by finite differences and convective boundary conditions are applied at $x = 0$ and $x = L$. The heat flux transferred by convection needs to be equal to the one transferred by conduction.

$$-k_t \left. \frac{dT}{dx} \right|_{x=L} = h_{RBS} [T(L) - T_{\infty}^{RBS}] \quad (3.2a)$$

$$-k_t \left. \frac{dT}{dx} \right|_{x=0} = h_{COS} [T_{\infty}^{COS} - T(0)] \quad (3.2b)$$

h_{RBS} and h_{COS} are the convection coefficients of the surroundings environments at a certain temperature T_{∞}^{RBS} and T_{∞}^{COS} , respectively. The values are imposed but depend on the situation studied.

3.1.2 Radiative transfer

The RTE represents the effects on the radiation intensity in a medium. The change on the intensity of radiation in a direction \hat{s} (left term of the Equation (3.3)) is due to emission, absorption, and scattering into and away of the direction considered (right terms for this order in Equation (3.3)).

$$\frac{dI}{ds} = kI_b - kI - wI + \frac{\sigma_s}{4\pi} \int_{4\pi} I(\hat{s}_i) \Phi(\hat{s}, \hat{s}_i) d\Omega_i \quad (3.3)$$

The absorption coefficient (k) is a volumetric radiative property of the material representing the effect of absorption/emission inside the medium. A transparent or non-participating medium is a medium with no participation in radiation and therefore with an absorption coefficient equal to zero.

Several assumptions are considered on the development of the model. The medium has a reduced thickness and is considered isotropic and homogeneous. Consequently, does not scatter significantly ($\sigma_s = 0$) and therefore the scattering albedo is also equal to zero ($w = 0$). This assumption is also considered in other studies for similar materials [51].

The RTE is usually written in terms of the optical coordinate (τ_L). This dimensionless parameter

is the integration of the extinction coefficient (scattering plus absorption) along the direction s . The absorption coefficient is considered constant along the direction and therefore the following relations are valid:

$$\begin{aligned}\tau_L &= \int_s (k + \sigma_s) ds = ks \\ d\tau_L &= k ds\end{aligned}\quad (3.4)$$

The intensity of radiation is spectral and the RTE is valid for a specific wavelength (λ). Comprising the simplifications, the RTE can be rewritten in a spectral form as:

$$\frac{dI_\lambda}{d\tau} + I_\lambda = I_{b,\lambda}\quad (3.5)$$

The radiation intensity is divided in positive (upwards) and negative (downwards) as represented in Figure 3.3. This notation is commonly used to simplification of calculus.

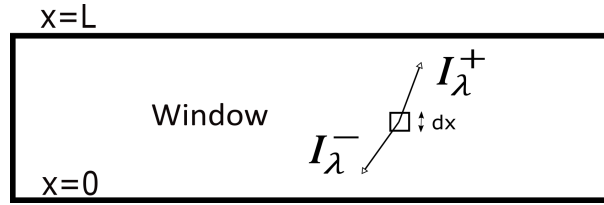


Figure 3.3: Schematic representation - Intensity radiation.

The direction of radiation is a parameter that needs to be considered. The solution method used in this work is the DOM. The main idea of the model is the substitution of the integration of intensity in all directions by the summation of numerical quadrature of discrete different directions. This model relies on the angular discretisation since it is an approximation by summation.

$$\int_{4\pi} I(x, s) d\Omega = \sum_{i=1}^n w_i I(x, s_i)\quad (3.6)$$

The quadrature weights (w_i) and the direction cosines (μ_i) are values which depend the dimension of study (one-dimensional slab) and the angular discretisation [9].

The RTE (Equation (3.5)) can be divided and solved using an integrative factor. The term related with the emission of radiation (I_b) is considered constant along the window due to non-significant differences in the temperature inside the medium. The following equations (3.7a and 3.7b) describe the spectral radiation intensity inside the medium to the case studied.

$$I_\lambda^+(\tau, \mu) = I_{b,\lambda}(\tau, \mu) + [I_\lambda^+(0, \mu) - I_{b,\lambda}(\tau, \mu)] e^{-\frac{\tau}{\mu_i}}\quad (3.7a)$$

$$I_\lambda^-(\tau, \mu) = I_{b,\lambda}(\tau, \mu) + [I_\lambda^-(L, \mu) - I_{b,\lambda}(\tau, \mu)] e^{-\frac{\tau_L - \tau}{\mu_i}}\quad (3.7b)$$

The emitted radiation for a black body is theoretically and experimentally defined by Plank [52] :

$$E_{b,\lambda}(\lambda, T) = \frac{C_1}{\lambda^5 \times (e^{C_2/\lambda T} - 1)} \quad (3.8)$$

where $C_1 = 3.742 \times 10^8 \text{ W}\mu\text{m}^4/\text{m}^2$ and $C_2 = 1.439 \times 10^4 \mu\text{m}/\text{K}$.

Figure 3.4 represents graphically the Plank function (Equation (3.8)), the emitted radiation as function of wavelength and temperature.

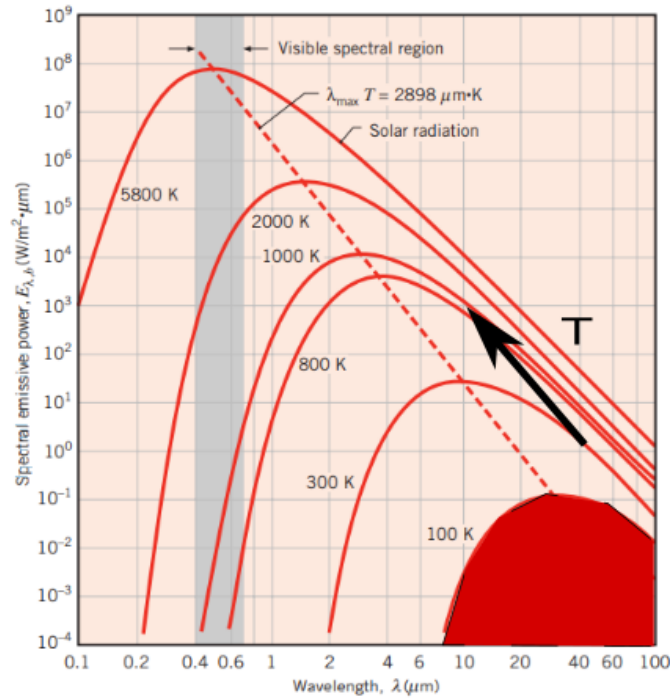


Figure 3.4: Plank distribution - Emitted radiation as function of wavelength and temperature (adapted from Reference [53]).

The spectral distribution of radiation intensity depends on temperature. The emitted radiation increase when temperature increase (black arrow in Figure 3.4). The emissive power can be calculated according with the integration of the emitted radiation along the wavelength band considered. The total emissive power is the integration considering the entire wavelength (red area in Figure 3.4) and depends also on temperature. The Stefan-Boltzmann law defines the relation of total emissive power with temperature:

$$E_b = \sigma T^4 \quad (3.9)$$

where σ is the Stefan-Boltzmann constant, equal to $5.67 \times 10^{-8} \text{ W}/\text{m}^2\text{K}^4$.

The equation presented represents the behaviour of emission for a black body. A black body is an idealization which absorbs all the radiation (ideal absorber) and for a specific temperature and wavelength, the body emits the maximum possible (ideal emissor). The model developed for this work is

not based on a black body but on a real body. The real bodies are defined according with an certain emissivity (ϵ). Emissivity is the fraction of the real emitted radiation compared with the emitted by a black body. This property is a intrinsic radiative property of the material depending on the wavelength and temperature.

The properties of the materials considered for this model are spectrally dependent and cannot be considered constant for the entire band since is a rough approximation as will be further demonstrated. For that reason, the problem demands a non-gray model. The non-gray model considers the emissive power of each wavelength band instead the total emissive power. The emissive power of a specific wavelength band is the integration of the spectral emitted radiation for that specific wavelength band and the Stefan-Boltzmann law cannot be directly applied since it computes the total emissive power. The strategy consists in applying a factor (F) to the total emissive power.

$$E_{\lambda_1-\lambda_2} = E_b \times F_{\lambda_1-\lambda_2} \quad (3.10)$$

Factor that is a fraction of the emissive power of the wavelength band compared with the total emissive power. The fraction depends on the range of the wavelength band considered and is written according with the definition of fraction:

$$F_{(\lambda_1-\lambda_2)} = F_{(0-\lambda_2)} - F_{(0-\lambda_1)} = \frac{\int_0^{\lambda_2} E_{\lambda,b} d\lambda - \int_0^{\lambda_1} E_{\lambda,b} d\lambda}{\sigma T^4} \quad (3.11)$$

The irradiation field (G) is then computed integrating the incoming intensity of radiation in all directions. The integration in all directions is substituted by a summation according with the DOM.

$$G_\lambda(x) = \int_{4\pi} I_\lambda(x, \hat{s}) d\Omega = \sum_{i=1}^{N/2} w'(i) (I_\lambda^+(x, i) + I_\lambda^-(x, i)) \quad (3.12)$$

The local divergence of the radiative heat flux is a balance, the difference of the emitted intensity and incoming radiation (irradiation). The divergence of the radiative heat flux is totally defined and can be inserted in the energy balance of the medium (Equation (3.1)).

$$\left(\frac{dq_r}{dx} \right)_\lambda = k_\lambda (4\pi \times I_{b,\lambda}(x) - G_\lambda(x)) \quad (3.13)$$

Boundary conditions

Boundary conditions are mandatory to solve the RTE ($I^+(0)$ and $I^-(L)$ in Equation (3.7a) and (3.7b), respectively). Figure 3.5 represents the three different contributions of boundary radiation to the medium (transmission, emission, and reflection). The radiation intensity of the boundaries is then divided into those three different terms and then combined into one term. The enclosure surfaces are not opaque surfaces and therefore are considered as semi-participating which allow the penetration of the outside radiation (G), emission (E) and reflection of radiation (H), see Figure 3.5. The scheme of Figure 3.5 only represents what is happening in one boundary ($x = L$) but the procedure is analogous on the opposite boundary ($x = 0$).

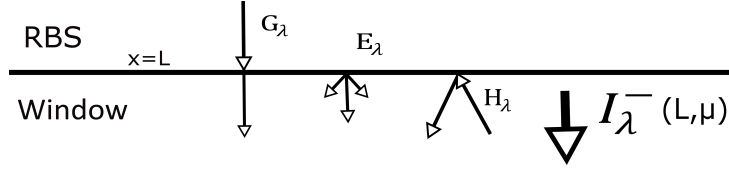


Figure 3.5: Schematic representation - Intensity radiation on boundary $x = L$.

The radiation of the boundary is then computed based on the radiosity (J). The radiosity represents the sum of the total radiant flux leaving the surface into the medium.

$$I_{\lambda}^{+/-} = J_{\lambda} \times \pi \quad (3.14)$$

The previous equation and the followings are only valid for diffuse surfaces since there is no dependence of radiation intensity on the direction. The behaviour is considered as isotropic and therefore the assumption is valid. The total radiosity can be computed according with the three different contributions.

$$J_{\lambda} = \tau_{\lambda}G_{\lambda} + \epsilon_{\lambda}E_{\lambda} + \rho_{\lambda}H_{\lambda} \quad (3.15)$$

The first term of Equation (3.15) ($\tau_{\lambda}G_{\lambda}$) is related with the penetration of the radiation coming from the outside. The term is related with the radiation coming from the burners to $x = L$ and with the radiation coming from the coil to $x = 0$. The emitted radiation of the burners/coil is equal to the received at the top/bottom surface of the window. The gases inside RBS and COS are considered as non participative to the radiation. This is an assumption since the molar fraction of CO_2 and H_2O (species that are reactive to radiation) is very reduced.

The radiation which penetrates the window is hence connected with the emitted radiation from the burner/coil:

$$G_{\lambda} = \epsilon_{bur/coil,\lambda} \times E_{bur/coil,\lambda} \quad (3.16)$$

The emissivities of the burner/coil are intrinsic properties of the materials considered for the surfaces and the emissive power accounts the emissive power of each wavelength band considered, directly related with the temperature of the coil/burners, initially imposed boundary conditions to the model.

The burner's radiative output is known and a treatment of data is necessary to transform it into a temperature imposed. A detailed explanation of the procedure is in the following subsection.

The coil temperature is estimated and imposed. The metal strip is continuously fed into the curing oven and an average between the temperature at which enters and leave the system is imposed for the reference case.

The second term of Equation (3.15) ($\epsilon_{\lambda}E_{\lambda}$) is related with the emitted radiative power of that surface. The third term of Equation (3.15) ($\rho_{\lambda}H_{\lambda}$) is related with the radiation from the medium, which is reflected again into the medium. This term is not initially known since the radiation coming from the medium is an unknown. The model developed include this term on a second calculus. The irradiation field is first calculated only based on the first two terms and then with the intensity field computed, the third term

$(\rho_\lambda H_\lambda)$ is obtained. The renewed boundary conditions are included again on the calculus of the renewed field of radiation intensity. The Equation (3.17) describes the calculus of this term based on DOM.

$$H_\lambda = \int_{\hat{n} \cdot \hat{s} < 0} I(x = 0/L, \hat{s}') \left| \hat{n} \cdot \hat{s}' \right| d\Omega' = \sum_{i=1}^{N/2} w'(i) I_\lambda^{+/-}(i) \quad (3.17)$$

where \hat{n} is the surface normal and \hat{s}' is the incoming direction.

The radiosity (J_λ) depends on the radiative properties of the surface considered (emissivity - ϵ_λ ; reflectivity - ρ_λ ; and transmissivity - τ_λ) (Equation (3.15)). The window is a participating medium to the radiation and considering a balance to the irradiation field, the field can be reflected, absorbed or transmitted. According with the definition of the radiative properties:

$$\alpha_\lambda = 1 - \rho_\lambda - \tau_\lambda \quad (3.18)$$

The emissivity is equal to the absorptivity by the Kirchhoff law. This equality is valid without restrictions for spectral and directional properties. A valid assumption since the model developed is non-gray and diffuse surfaces are considered, independent of direction.

The absorption coefficient (k) is a volumetric property of the medium, independent of the thickness of the material and transmissivity is a surface property, which has dependence on the thickness of the material. Considering normal incident radiation, the transmissivity can be defined by the Beer's law [54]:

$$\tau_\lambda = e^{-k_\lambda \times L} \quad (3.19)$$

The reflectivity of a surface depends directly on the index of refraction of the surrounding media. RBS and window are the surrounding media considering the top surface, COS and window considering the bottom surface. The media of RBS and COS are considered with index of refraction equal to 1 since the media do not disturb the radiation field. Assuming the incoming radiation is perpendicular, which is a good assumption since the bodies (burner, surface and coil) are parallel with each other. Fresnel equation [55] can be simplified to compute the reflectivity of the surface:

$$\rho_\lambda = \left| \frac{n_\lambda - 1}{n_\lambda + 1} \right|^2 \quad (3.20)$$

The boundary conditions and the field of radiation intensity in RTE is then analytical totally defined.

Burner surface temperature

The burner is the radiative source. The IR porous burners are based on a combustion process and have a radiative and an advective contribution. The advective contribution comes from the output of the combustion by the gas expelled and the radiative contribution is directly connected with the temperature and emissivity of the burner porous surface. The radiative efficiency of the burner influences the surface temperature of the burner (T_{bur}). The emissivity of the surface ($e = 0.9$) is known since the material used is known.

The solution to impose the temperature of the burner is linked with the information known of the burner's power, which is dependent on operating condition. The cases studied along the work consider a nominal operating condition for one burner of 25 kW (sum of radiative power with the advective power - P_{bur}). The radiative contribution (Y_{rad}) depends on several factors but it was assumed as equal to 0.3 along the study.

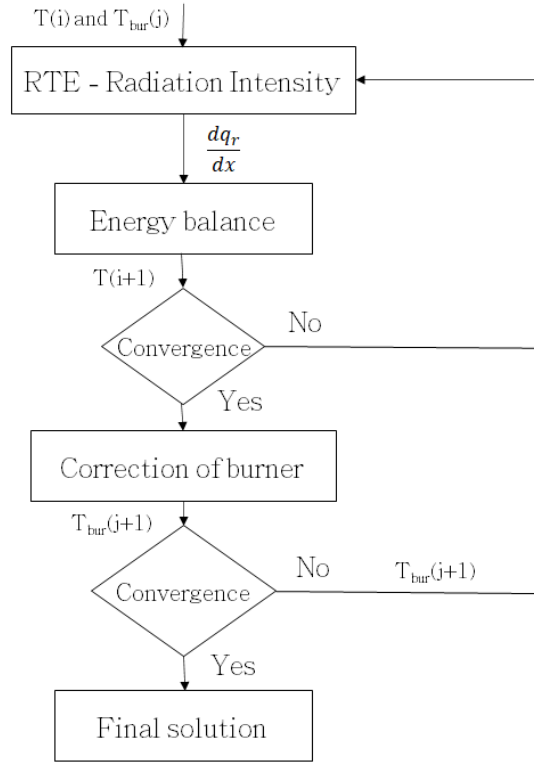


Figure 3.6: Flow chart of model developed.

The model includes the previous information in an outer iterative procedure as described in flow chart of Figure 3.6. The model matches the radiative flux calculated by reducing or increasing the surface temperature of the burner. The model calculates iteratively the difference (Δ) between the calculated radiative flux coming from the burner's and the reference case. (see Equation (3.21)). The model then changes the temperature imposed to the burner according with that difference and a factor (f) which is variable (see Equation (3.22)).

$$\Delta(i) = q_r(i) - \frac{Y_{rad} \times P_{bur}}{A_{bur}} \quad (3.21)$$

$$T(i+1)_{bur} = T(i)_{bur} + \Delta(i) \times f \quad (3.22)$$

This is an outer iterative process after the convergence of the coupling between energy equation and RTE. A convergence criteria is achieved when residual defined as the difference of surface temperature is less than 10^{-3} .

Figure 3.7 shows a example of the model adjustment to the surface burner temperature based on the radiative flux and efficiency previously defined.

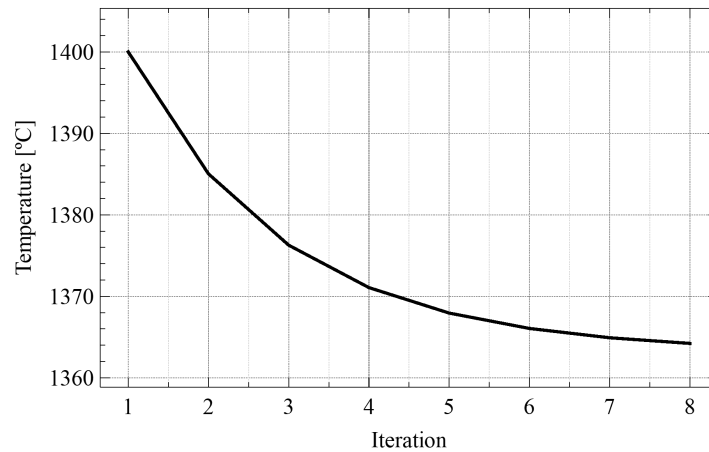


Figure 3.7: Burner's surface temperature with iterations.

3.1.3 Convective heat transfer correlations

The convective heat transfer on the glass surfaces is imposed by a convection coefficient (h) and a surroundings temperature (T_∞) - Equation (3.2a).

Nusselt number is a dimensionless dimension and commonly defines the convection coefficient as:

$$\overline{Nu} = \frac{\overline{h}L}{k_t} \quad (3.23)$$

where L is defined as a characteristic length. The average Nusselt number is evaluated since the study is focused on the one-dimensionality of the window. Nusselt number can be empirical, analytically or numerically defined.

Situation without cooling

The fluid flow and heat transfer conditions without cooling inside RBS can be approximated as an impinging jet onto a plate - see Figure 3.8. Zuckerman and Lior [56] review several studies of impinging jets, and provided correlations for both local and average Nusselt numbers.

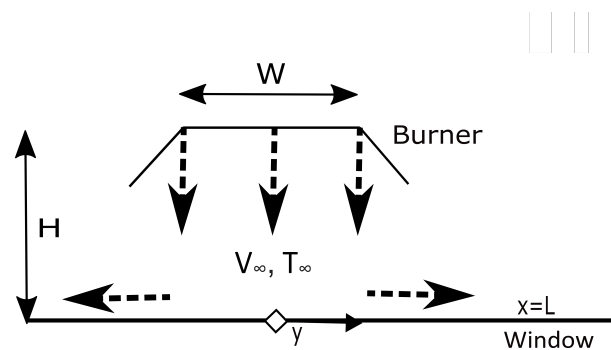


Figure 3.8: Schematic representation - Impinging jet against the window.

The most adequate empirical correlation to the current model and to the conditions of the system is provided by the study of Martin [57] for a slot nozzle:

$$\overline{Nu} = Pr^{0.42} \times Re^m \times \frac{3.06}{0.5/A_r + H/W + 2.78} \quad (3.24)$$

where A_r is a geometrical parameter referred to $W/2y$, W is the length of the slot nozzle and y is the limit distance of the domain of study, starting from the stagnation point, and $m = 0.695 - \left[\left(\frac{1}{4A_r} \right) + \left(\frac{H}{2W} \right)^{1.33} + 3.06 \right]^{-1}$.

The gas is composed in a molar basis by different species such as N_2 (70%), CO_2 (7%), H_2O (12%), and O_2 (3.6%). Sutherland's model provided absolute viscosity and thermal conductivity for the specific species of the gas [58]. The specific heat of the species were evaluated with polynomial functions depending on the temperature according with technical database [59]. The properties of the gas are temperature dependent and the temperature considered in the evaluation of the properties depends also on window temperature. The gas properties are evaluated at an average temperature between inlet gas and window temperature as commonly applied in heat transfer studies [53]. The solution of the problem is integrated on the iterative process of the coupling between RTE and energy equation (Flow chart of Figure 3.2), where the gas properties are evaluated with the renewed field of window temperature. The temperature of the environment (T_∞) is defined as equal to the gas temperature at burner's output (1340 K).

COS is a section where there is no impinging jet applied and the values of heat transfer convection coefficient are estimated to a situation of natural convection ($h_{COS} = 10 \text{ W/m} \cdot \text{K}$) and an average temperature considered ($T_{COS} = 425^\circ\text{C}$).

Situation with cooling

The cooling mechanism affects directly the convection inside the media and the convection coefficients need new evaluation. These parameters need to be defined and depend on the intensity of external cooling performed by a cooling slot on the glass surface. The cooling jet is injected parallel to the window as wall jet. The conditions of the system (backward-facing step at the entrance - 3 times the jet height and perpendicular wall at the end of the wall) demonstrate a very specific situation which correlations already studied become not suitable for the situation considered (see Figure 3.9). The strategy to obtain a valid correlation for the specific situations studied was simulate the case numerically. The geometrical model of RBS is simplified - half of one row of burners - due to symmetric conditions (see Figure 3.9). The case with cooling inside COS is similar but does not register burner's output.

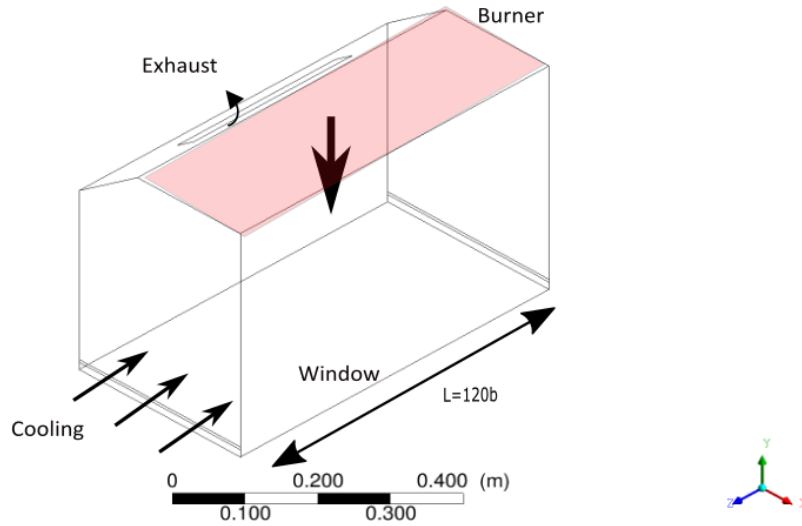


Figure 3.9: RBS geometric model of half battery of burners without the window.

The mathematical and physical models used are the ones used in Section 2.1. The turbulence model of SA closes the RANS equations. This turbulence model provided reliability for the study of wall jets, as demonstrated on the previous chapter. The model has a very reduced grid size near the wall due to necessary low-Re modeling. The numerical model simulated fixes the impingement conditions as nominal burner's output ($v_{gas} = 1.975$ m/s and $T_{gas} = 1340$ K) and varies the operating conditions of cooling (Reynolds number by manipulating the velocity and fixing the cooling gas injection temperature ($T_{COS/RBS}$)). An uniform temperature of the window is prescribed (T_w). The studies on heat transfer in wall jets considered an iso-thermal wall [23] and AbdulNour *et al.* [22] concluded that there is no difference by considering an iso-thermal or iso-flux surface. The lateral walls parallel to plane YZ are considered with symmetric boundary conditions and the remain walls are considered adiabatic.

The importance of the mesh size is investigated inside RBS and 5 different meshes are simulated. Figure 3.10 shows that a mesh with 2.25×10^5 cells provides a compromise between accuracy and computational effort, with a error of only 0.2% in relation to the most refined mesh.

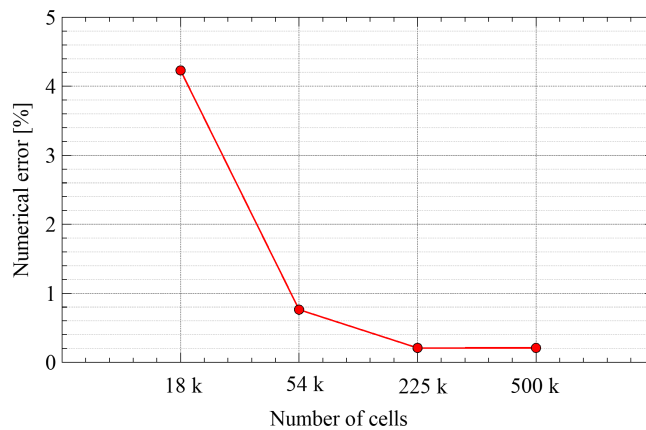


Figure 3.10: Numerical error associated to wall jet cooling inside RBS.

The local heat transfer on the surface of the window is then analyzed and the coefficient of heat transfer over the target surface, was normalized for an isothermal target surface, with the inlet jet temperature being the reference temperature ($T_{COS/RBS}$) [48]:

$$h = \frac{q_c}{T_w - T_{COS/RBS}} \quad (3.25)$$

The correlation can be then defined as literature reports for wall jet cooling:

$$\overline{Nu} = f(Re) = C_1 \times Re^{C_2} \quad (3.26)$$

The properties are considered at an average temperature between inlet cooling gas temperature and window temperature. The jet height (5 mm) is the reference length which defines Nusselt and Reynolds numbers.

The different cooling strategies presented in Section 1.2 were simulated for RBS and COS, separately. The cooling scheme C has a variation of side along the window (see red arrows in Figure 4.5(c)). The variation of side is defined at half of one of burners and consequently, the geometrical model inside RBS demanded the double of the model represented in Figure 3.9.

The same strategy was used to simulate the cooling inside COS and due to geometrical simplifications, cooling schemes A and B could be simulated as 2D. The results are represented in Table 3.1.

Table 3.1: Coefficients for heat transfer correlation.

	RBS			COS		
	A	B	C	A	B	C
C_1	0.0048	0.0058	0.0037	0.0077	0.0088	0.0087
C_2	0.838	0.795	0.867	0.819	0.800	0.784

The comparison between strategies should be performed at the same mass flow rate and not velocity. For the same mass flow, the velocity at injection on both sides (cooling scheme B) is reduced to half. Consequently, the Reynolds number associated to cooling scheme B is the double for better comparison purposes.

The results show that the coefficient C_2 is almost equal to 0.8 for all numerical simulations. The results are consistent due to cooling behaviour being as wall jet - Equation (1.1). The coefficient C_1 is higher inside COS than RBS due to absence of impingement jet of burner's output, which reduces the heat transfer inside RBS.

The results of the correlations inside RBS are graphically displayed in Figure 3.11 for better comparison. There are no significant differences between cooling scheme A and C, only at reduced Reynolds. Cooling scheme B predicts a reduced Nusselt number for the same Reynolds.

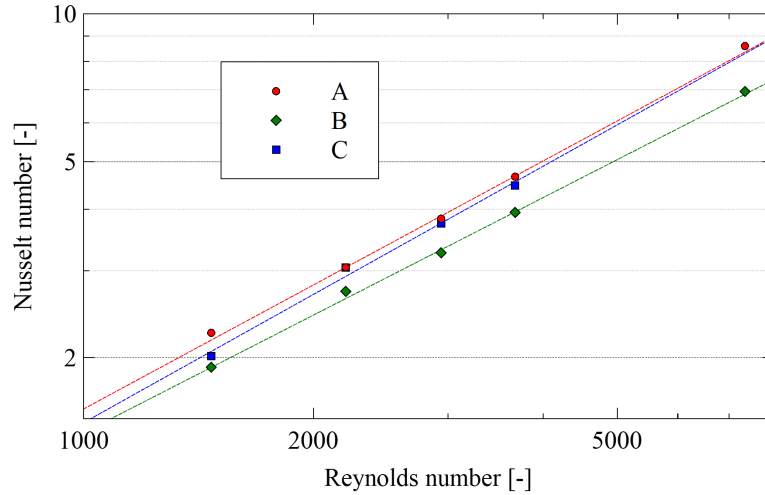


Figure 3.11: Numerical average heat transfer correlations for different cooling schemes inside RBS.

3.1.4 Verification

The verification process ensures that the equations are solved correctly, by performing a comparison with reference studies. The window model is herein verified against literature data and results predicted by a commercial software.

Literature

The window model developed is herein compared with a reference study of radiation and conduction model in a semi-participating medium [6]. Commonly dimensionless parameters are usually evaluated on these heat transfer studies:

- Conduction-radiation parameter, N

$$N = \frac{k_t \times k}{4\sigma T_{ref}^3} \quad (3.27)$$

Conduction-radiation parameter is a dimensionless parameter which provides a relation between the two transfer modes (conduction and radiation). High N means that the dominant transfer mode inside the medium is the conduction and in a hypothetically case ($N = \infty$) the heat transfer is ruled only by conduction. The opposite happens when N equals to 0.

- Optical thickness, τ_L

Optical thickness is an optical property which is related with the absorption inside the medium and the thickness. The parameter is identified by the product between the thickness and the absorption coefficient only in a medium where absorption coefficient can be assumed as constant along the thickness.

- Non-dimensional temperature, θ_L

The temperature profile inside the medium is dimensionalized by the maximum temperature inside the medium.

The temperatures are fixed on the boundaries ($\theta_L = 1$ and $\theta_L = 0.5$) and there is no penetration of the outside radiation since the boundaries are not simulated as semi-transparent, but as diffuse opaque boundaries. The boundary conditions of the study also do not reflect ($\epsilon = 1$).

The results obtained are shown in Figure 3.12. The lines without marks represent the values obtained with the current model and the lines with marks represent the results from reference as the legend indicates. The comparison between the models is for identical situations: same optical thickness (two different figures for different optical thickness); and for different N (different lines inside the figures).

The difference between the models occurs when N is very reduced and when the optical thickness is high. The model implemented shows lack of accuracy for that cases since the model developed assumes the term related with the emission of radiation constant along the window (Equations (3.7a) and (3.7b)) due to no significant differences of temperature inside the window - case that will be the focus of study. A reduced N means that the radiative contribution has higher impact than conduction and a higher optical thickness means the material absorbs more radiative energy. The situations that will be the focus of the work do not register so reduced values of N . The reference case registers values of $N = 13.2$ and $\tau_L = 0.92$. For those situations, the results are similar as the graphs show. The previous information provides confidence on the current model used to perform the study. There is a perfect match for the different situations of $\tau_L = 0.1$. The increase of the optical thickness leads to a less linear profile as expected since the radiation has a higher impact on that medium (Figure 3.12(a) compared with Figure 3.12(b)).

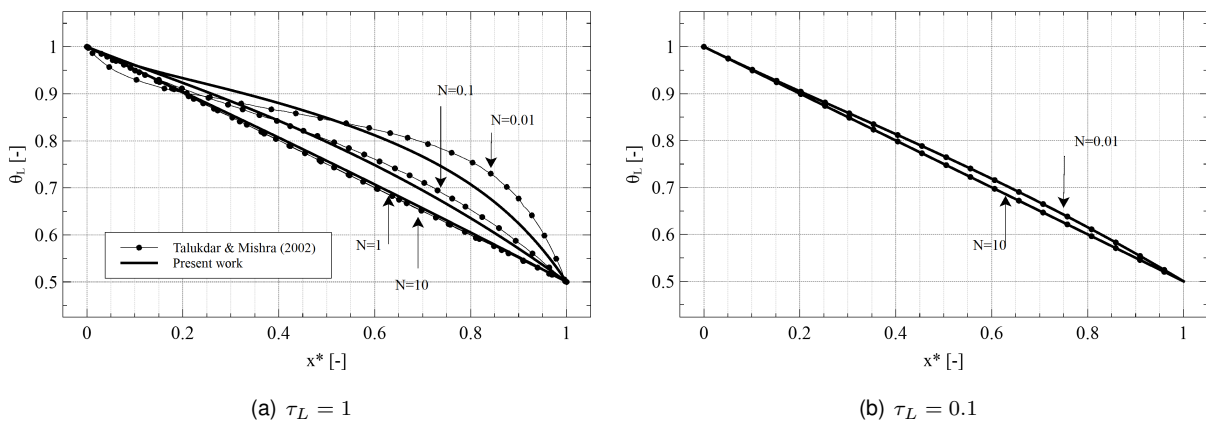


Figure 3.12: 1D window model validation.

The reflection is an important part of the study in participating media as windows and that is integrated in this comparison study. Figure 3.13 shows the results obtained for a case when N is equal to 0.1 and $\tau_L = 1$. There is a slight difference between the reference values and the ones obtained by the model as already explained. The conclusion from this comparison is that the difference between cases with different emissivities is almost the same. The difference between the black lines in Figure 3.13 is

almost the same as the difference registered with the current model (marked lines in Figure 3.13).

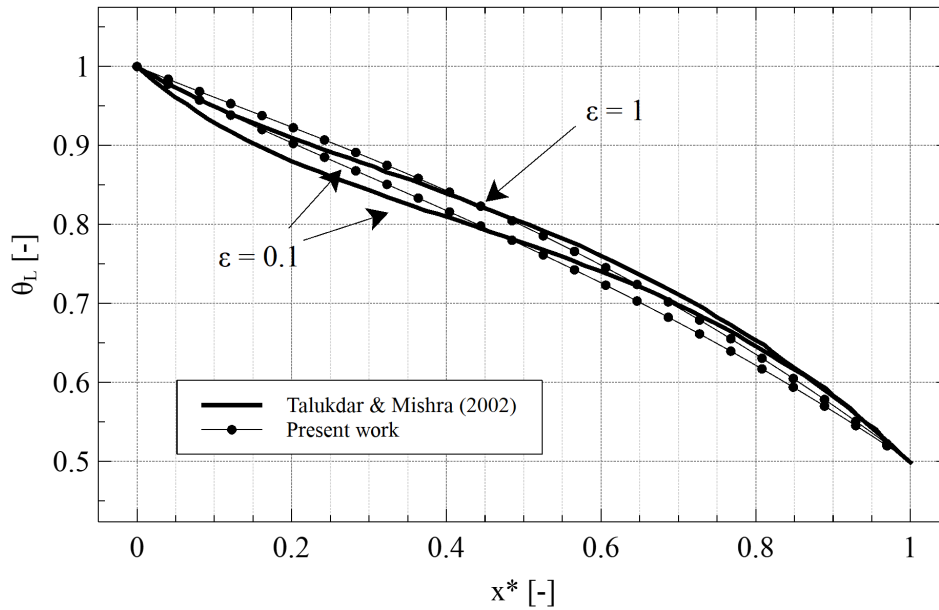


Figure 3.13: 1D window model validation for different emissivities.

The main conclusion from the comparison is that the model developed with an iterative coupling and DOM shows the expected behaviours for a conduction-radiation heat transfer and accurate results for the situations that will be the focus of study.

Commercial software-2D model

The comparisons here addressed are focused on verify the 1D model developed. The purpose is to check if the current model has similar results to a 2D model. The 2D glass window model was implemented in a commercial software, ANSYS Fluent.

The window is simulated close as possible to the 1D reference case. The commercial software allows the implementation of boundary conditions for radiation and convection on the surfaces where there is penetration and contact with fluid media, RBS and COS. The algorithm used on the development of the model to impose radiative flux instead temperature was not included in this comparison. A burner surface temperature equal to 1400°C was then prescribed. The lateral walls are assumed as symmetric and the y dimension is equal to the x distance. The commercial software does not take into account the emission from the surface, only with the penetration of outside radiation and with reflection [60]. The DOM used had a similar angular discretisation (4 divisions in θ) and the same spatial discretisation (almost 100 cells for each 2 mm of the window). The comparison was performed to the situation without cooling on both sections (RBS and COS). The 2D model does not consider the numerical simulation of surrounding environments but the convection coefficient and surrounding temperature, equal to the 1D model. The computed convection coefficient by the model developed (correlation of impingement jet) provided this value as basis to Fluent.

Results were considered when the residuals from DOM and energy equation were below 10^{-6} . The

result of the simulation for a 2 mm window is represented in Figure 3.14. The result of the commercial software comply with the expectations since the hottest zones are at the upper surface and the coolest at the bottom surface. The profile is non-linear due to absorption and very similar to the one obtained with the current model.

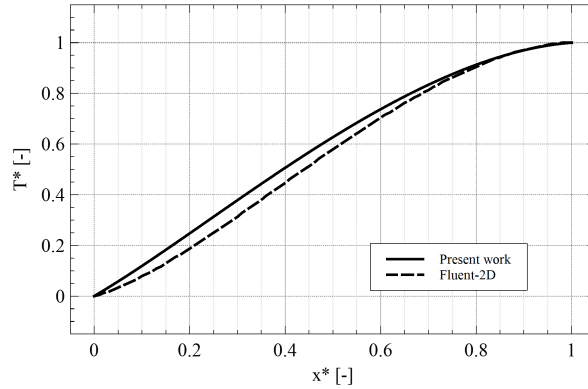


Figure 3.14: Comparison of nondimensional temperature profiles between current model and ANSYS Fluent.

The dimensionless profiles show similar profiles but the magnitude of the average window temperature and absorbed thermal power ($\overline{T_w}$ and \dot{q}) are also inspected. The results are displayed in Table 3.2 and show similar solutions for the two different cases. The absorbed thermal power increases when the thickness increases. The difference between temperature and adsorbed power is higher in 1D model when comparing a 2 mm with a 5 mm window. The 1D model developed includes the emission from the surface, which is dependent on the temperature.

Table 3.2: Comparison of average window temperature and absorbed power between 1D model developed and 2D model in ANSYS Fluent for two window thicknesses.

Thickness	1D		2D - Fluent	
	$\overline{T_w}$ [°C]	\dot{q} [kW/m ²]	$\overline{T_w}$ [°C]	\dot{q} [kW/m ²]
2 mm	916.0	4.14	933	4.61
5 mm	1017.0	5.67	1000.0	5.78

3.2 Results

The model developed can predict the thermal behaviour of the window. The following section intends to analyses the effects of different parameters on its behaviour.

3.2.1 Reference case

The developed 1D model computes the temperature distribution and provide information regarding the thermal performance of the window. The model is focused on computing the temperature distribution inside the window for specific input parameters (design and operating conditions). The model considerations (spatial, angular, and spectral discretisation) are also considered as an input to the program.

Table 3.3 displays the parameters considered for the reference case. The reference case is similar as possible to the real model in order to comply with the objectives of the work.

Table 3.3: Input parameters for reference case.

Design and operating conditions-Input parameters							
Burner	Number of points	100	COS	Convection coefficient, h_{COS} [$W/m^2 \cdot K$]	10		
	DO model	S4		Surrounding temperature, T_{COS} [K]	700		
	Radiative efficiency, Y_{rad} [-]	0.3		Number of wavelength bands	3		
	Emissivity, ϵ_b [-]	0.9	Window	Range of wavelength, [μm]	0-5	5-6.3	6.3-25
	Gas temperature, T_{gas} [K]	1340		Spectral absorption coefficient, k [m^{-1}]	7.2	228.9	973.7
	Gas velocity, v_{gas} [m/s]	1.975		Spectral index of refraction, n_λ [-]	1.69	1.58	1.31
Coil	Surface temperature, T_{coil} [K]	407.15	Thickness, L [mm]	2			
	Emissivity, ϵ_{coil} [-]	0.31	Thermal conductivity, k_t [$W/m \cdot K$]	8			

The results show the lowest temperature on the surface in contact with COS ($x^* = 0$) and the highest on surface with RBS ($x^* = 1$). The difference of temperature inside the medium is very small ($\Delta T = 1.04^\circ C$) due to the reduced thickness and thermal conductivity of the material considered. The absorption of energy and the surrounding media are the reason for the high temperatures of the medium ($\overline{T_w} = 889.2^\circ C$).

The model developed compute the local divergence of radiative heat flux, graphically displayed in Figure 3.15. The integration of the divergence of radiative flux (gray area in Figure 3.15) provide the total power absorbed by the window ($\dot{q} = 3.71 kW/m^2$). The negative values represent the zones where the emission is higher than absorption. Those zones are near $x^* = 0$ as it would be expected since the penetration of radiation is higher on $x^* = 1$, and consequently register the highest values of temperature. The integration is approximated by the trapezoidal method since there is no knowledge of the function but only local values.

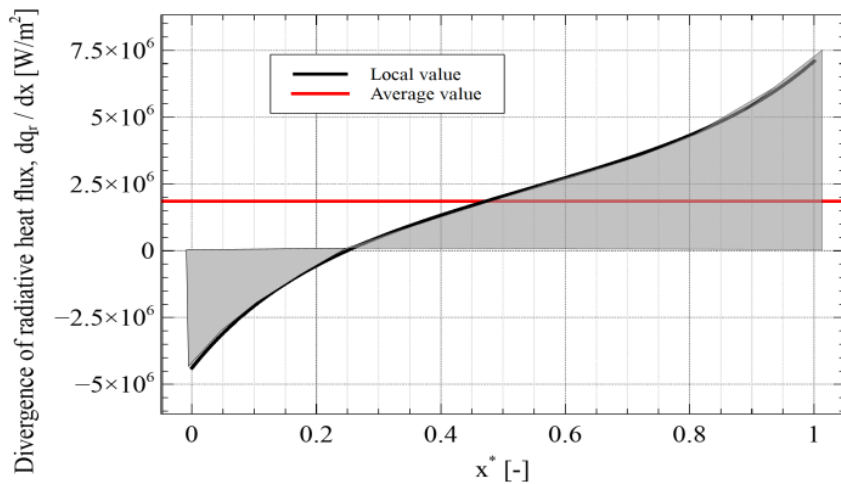


Figure 3.15: Local divergence of radiative heat flux inside the window.

The red line represents the average value and there is a high variation on the divergence of heat

flux across the thickness. The values near $x^* = 0$ and $x^* = 1$ have the triple of the magnitude when compared with the average. The average value is registered at the middle of the window, $x^* = 0.5$ (cross of both lines).

3.2.2 Effect of spatial, angular and spectral discretisation

The spatial discretisation is directly related with the accuracy of the model since the derivatives of the temperature are approximated by finite differences. The average temperature inside the window ($\overline{T_w}$) and the computational time for a laptop computer (i7-4720HQ processor) is the parameter analyzed and compared between the different simulations.

Table 3.4 lists the results of the parametric analysis to this parameter. The results show a small difference for meshes with more than 100 points.

Table 3.4: Relevance of spatial discretization on window model results and simulation performance: average window temperature and simulation time.

Number of nodes	10	50	100	200	1000
Avg window temperature, $\overline{T_w}$ [°C]	867.2	887.6	889.2	890.0	890.8
Computational time [s]	0.31	0.75	1.30	2.37	12.39

The angular discretisation is directly related with the DOM. The integration of all directions simplified by the summation over quadrature weights relies on the angular discretisation. S2 models represents a model simplified by considering two directions with the weight associated to all, S4 considers four directions and so on. The same method previously used on the evaluation of the spatial discretisation is here applied when evaluating the angular discretisation. Table 3.5 lists the results obtained. The results show that S4, S6 and S8 models predict very similar results and an adequate choice of the model is the S4 model.

Table 3.5: Relevance of DOM angular discretisation on window model results and simulation performance: average window temperature and simulation time.

DO Model	S2 symmetric	S2 non-symmetric	S4	S6	S8
Avg window temperature, $\overline{T_w}$ [°C]	859.1	888.7	889.2	888.9	888.7
Computational time [s]	1.05	0.80	1.30	1.81	2.34

The spectral discretisation is also a factor of interest. A gray model is defined by constant radiative properties for the entire spectrum while a non-gray model considers different wavelength bands. Increasing the number of wavelength bands leads to higher accuracy of the solution but also to higher computational effort.

Table 3.6 presents the results obtained for considering different wavelength bands for the reference case. The results show a high difference when considering different wavelength bands. The accuracy is evaluated by the average window temperature and the more reliable choice corresponds to 3 wavelength bands since the accuracy is compromised by considering lower number of bands. The computational effort increases 80% by considering 3 bands instead a gray model.

Table 3.6: Relevance of radiative properties spectral discretisation on window model results and simulation performance: average window temperature and simulation time.

Number of bands	1		2		3	
Wavelength range, λ [μm]	0-25	0-5.7	5.7-25	0-5	5-6.3	6.3-25
Absorption coefficient, k_λ [m^{-1}]	458.66	17.68	907.95	7.15	228.91	973.71
Index of refraction, n_λ [-]	1.51	1.68	1.34	1.69	1.58	1.31
Avg window temperature, \overline{T}_w [$^\circ\text{C}$]	931.0	982.8		889.2		
Computational time [s]	0.81	1.05		1.30		

3.2.3 Effect of window thickness

The thickness of the medium is a design parameter which has direct influence on the temperature of the medium since the medium absorbs radiative energy. The following analysis simulated the reference case for windows with different thicknesses. The spatial discretisation is the same, this means that the spacing between nodes is equal. The total number of nodes is different since the thickness differs for each case. For example, a 2 mm sample has 100 nodes associated and a 10 mm window has 500 nodes associated.

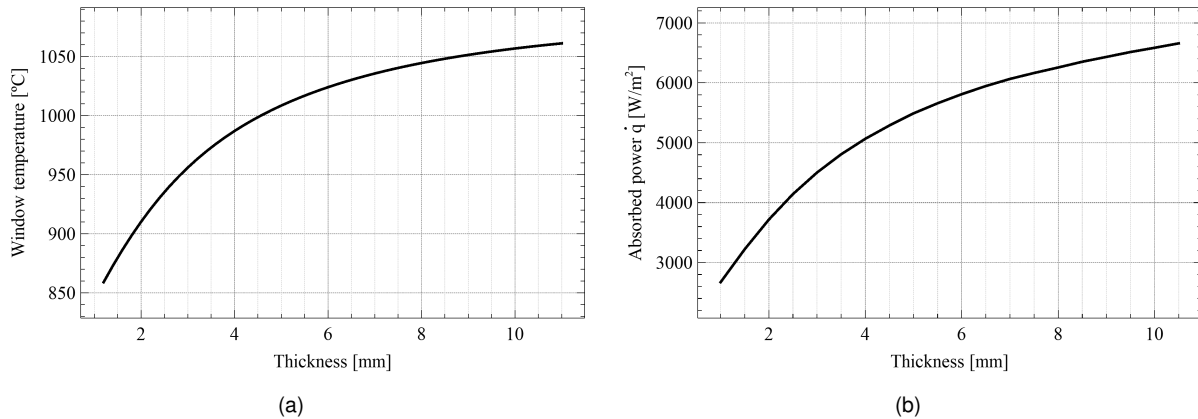


Figure 3.16: Window temperature (a) and absorbed power (b) with variable thickness.

Figures 3.16(a) and (b) present the window temperature variation and the absorbed thermal power, respectively, upon increasing the window thickness. The results show that an increase on the thickness leads to more radiative energy absorbed (Figure 3.16(b)) and therefore to a higher temperature (Figure 3.16(a)). The increase of temperature is logarithmic and similar to the increase of radiation absorbed. The increase of temperature is decaying with the increase of the thickness. A 4 mm sample registers 100 degrees higher temperature than a 2 mm window while a 6 mm sample has only 35 degrees higher than a 4 mm window.

3.2.4 Effect of window thermal conductivity

The thermal conductivity of the medium is an intrinsic property of the material considered and five media with a different thermal conductivity were analysed ($k_t = 0.1, 1, 4, 8$ and $40 \text{ W/m} \cdot \text{K}$). The fourth value matches the reference case.

The average temperature inside the medium does not change with the different materials (see Figure 3.17). The five different cases register almost the same temperature at the middle of the window. The non-linearity of the temperature profiles due to the absorption of radiation is more evident for the case with lower thermal conductivity since presents a higher gradient of temperature. The materials with lower thermal conductivity have lower temperatures near $x^* = 0$ and higher near $x^* = 1$. The results comply with the expectations since the thermal conductivity has an effect on the gradient of temperature.

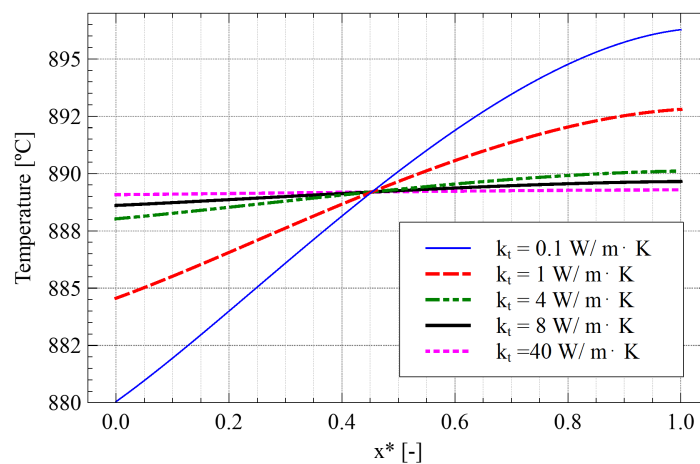


Figure 3.17: Temperature profile for materials with different thermal conductivity.

3.2.5 Effect of window radiative properties

The radiative properties of a window have an influence on the thermal performance of the window. The radiative properties of the medium influence the absorption of energy and therefore the temperature inside the medium. A highly absorbent material will absorb more energy and consequently register a higher temperature than a weakly absorbent material. A transparent window is the case when the medium is non-participating to radiation and therefore does not absorb any energy.

The radiative properties of the materials are defined by an absorption coefficient and an index of refraction, which are intrinsic properties of the material. Some materials do not have these intrinsic radiative properties available and the commonly used method in literature to obtain these values from experimental values is the analogous procedure developed in Section 3.1.2, based on Fresnel's and Beer's law (Equations (3.19) and (3.20)) and experimental values of reflection and transmission.

The reference material is compared with a transparent glass ($k = 0$), with soda lime silica glass [61] and another glass very similar to GE-214 quartz. The reference study regarding the soda glass provided direct information of the optical radiative properties and the glass is considered as the highly absorbent material since it has the highest absorption coefficient. The comparison study focused only on a range

until a wavelength of $5 \mu\text{m}$.

The temperature profiles displayed in Figure 3.18 are in accordance with the expectations. The profiles of temperature are non-dimensionalized by the maximum and minimum temperatures. The highly absorbent material (soda lime glass) absorbs more energy and therefore registers a higher temperature inside the window. The transparent material has a linear profile and registers the lower temperature since does not participate in radiation. The absorbent material has a higher optical thickness (around 0.6) and therefore the profile of the soda glass follows the curves of Figure 3.12(a) while the reference glass with lower optical thickness (around 0.01) follows the curve of Figure 3.12(b).

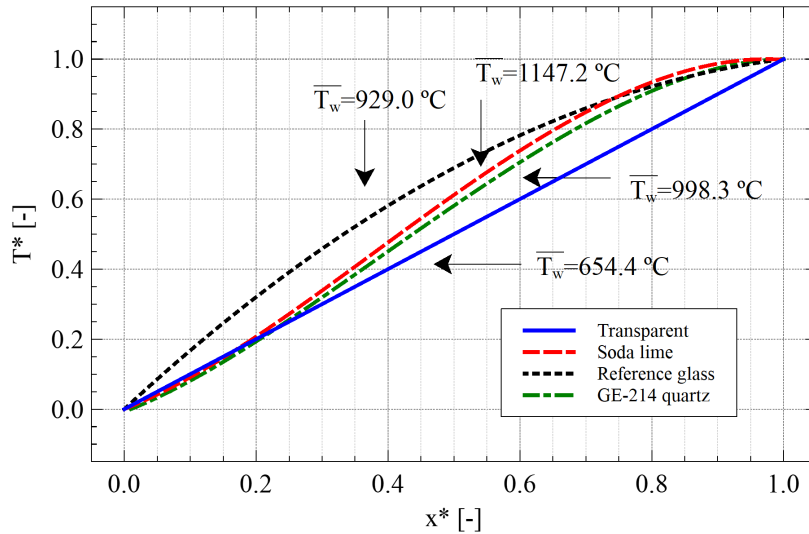


Figure 3.18: Temperature profile for material with different radiative properties.

3.2.6 Effect of surrounding surfaces

The emitted radiation from the surrounding surfaces is a parameter which has a influence on the temperature distribution inside the window. The following analysis is focused on studying that influence on the window. The two surfaces which enclosure the window are both inspected.

The influence of the coil was inspected by changing the temperature imposed (Initial temperature - 307.15 K - temperature at which the metal strip enters the oven; Final temperature - 507.15 K - temperature at which the metal strip exist the oven; and an average temperature - 407.15 K).

Table 3.7 shows the average temperature inside the window for the different cases. The window temperature increases when the temperature of the coil increases since the emitted radiation is higher and therefore the radiation absorbed of the window is higher. Nevertheless, the effect of the coil temperature is very reduced due to the reduced temperature of the coil and the reduced emissivity.

Table 3.7: Influence of coil temperature on window average temperature.

Coil temperature, T_{coil} [K]	307.15	407.15	507.15
Avg window temperature, $\overline{T_w}$ [°C]	888.3	889.2	891.1

The influence of burner's output is also analyzed in this section. Three different values of radiative efficiency were considered (0.3, 0.4 and 0.5). The radiative efficiency represents the fraction of radiative power compared with the total power of burner's output. Table 3.8 shows the burner's surface temperature adjusted as well the window average temperature.

The results are in accordance with the physical models and expectations. Increasing the radiative efficiency leads to higher burner surface temperature and therefore to higher temperatures inside the window since the absorbed energy is higher. This parameter has a high influence on the window temperature since the difference between changing from a efficiency of 0.3 to 0.5 leads to a difference of 209 degrees on the burner's surface temperature, which results on a increase of 137 degrees inside the window.

Table 3.8: Influence of burner's radiative efficiency on burner surface temperature and average window temperature.

Radiative efficiency, Y_{rad} [-]	0.3	0.4	0.5
Surface burner temperature, T_{bur} [°C]	1364	1477	1572
Avg window temperature, $\overline{T_w}$ [°C]	889.2	967.7	1035.1

3.2.7 Effect of cooling gas temperature and velocity

The cooling is applied on the model developed taking into account heat transfer information resulting of 3D numerical simulations of wall jets as described in Section 3.1.3. The objective of the study is to analyze the impact of cooling on both sections and the influence of operating conditions such as cooling gas temperature and velocity.

The cooling gas injection temperature defines directly the reference temperature (T_∞) and the cooling velocity defines the Reynolds number. The numerical correlations associate the Reynolds number to the heat transfer of wall jet. The case with the cooling scheme C applied inside RBS (only the red arrows in Figure 1.2(c)) is linked to the 1D model and the results are represented in Figure 3.19. Figure 3.19 shows that the highest window temperatures are observed for lower (higher) cooling gas injection velocity (temperature) values. The results also demonstrate the high impact of cooling inside RBS on the reduction of the temperature. The temperature can be reduced 400°C (889.2°C without cooling to 506°C) by a wall jet cooling with 25 m/s at 80°C.

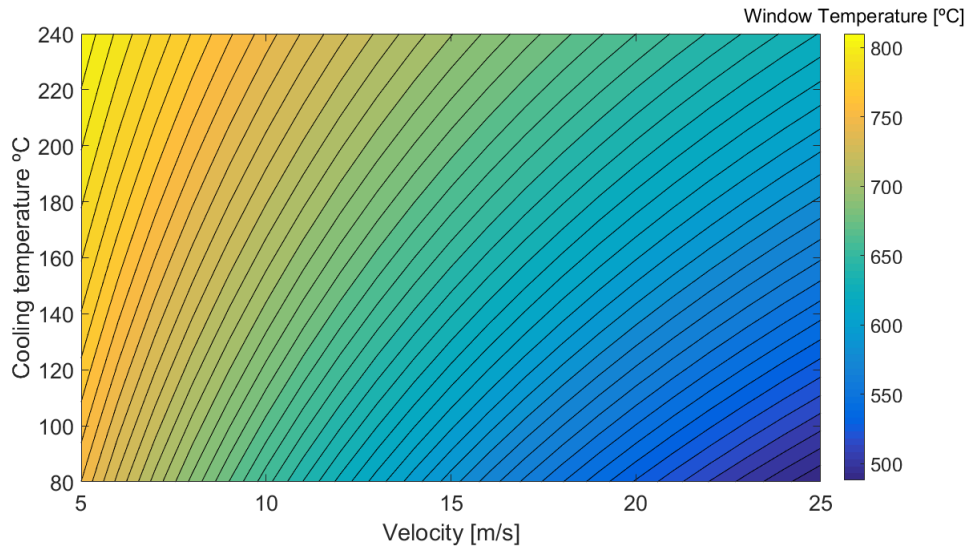


Figure 3.19: 2D contour plot of window temperature dependent of cooling gas injection velocity and temperature.

The analysis also makes a analysis of the temperature profiles inside the window for different situations: without cooling and with other two different levels of cooling velocity for COS and RBS (see Figures 3.20(a) and (b)). The nominal operating condition of cooling corresponds to 25 m/s at 80°C in RBS and 12.5 m/s at 250°C in COS (red dashed lines in Figure 3.20). The cooling applied inside COS has a reduced impact on the reduction of window temperature due to the reduced velocity ($v_{COS}=12.5$ m/s) and the higher temperature of cooling ($T_{COS}=250^{\circ}\text{C}$).

There is a clear difference of the temperature profile between the situation without cooling and with cooling inside RBS (see Figure 3.20(a)). Cooling applied on the surface $x^* = 1$ leads to a minimum on this surface (dotted lines). There is a slight difference on the temperature profile for the different cases of cooling. Increasing the mass flow rate of cooling leads to a lower temperature inside the window, a higher conduction-radiation parameter and therefore a more linear temperature profile. The dimensionless temperature profiles are very similar when the cooling is applied inside COS (see Figure 3.20(b)).

The combined effect of cooling (RBS and COS) is also studied and the results are displayed in Figure 3.20(c). Cooling applied on both surfaces leads to a maximum of temperature inside the window for all the cases studied due to absorption of radiation. The cases with a higher velocity on a region (red and pink lines) leads to the minimum on that surface. The profiles are not symmetric due to the different characteristics of both regions (cooling gas temperature and burner's output). The use of combined cooling leads to a reduced average window temperature for the nominal operating condition ($\overline{T_w} = 446^{\circ}\text{C}$).

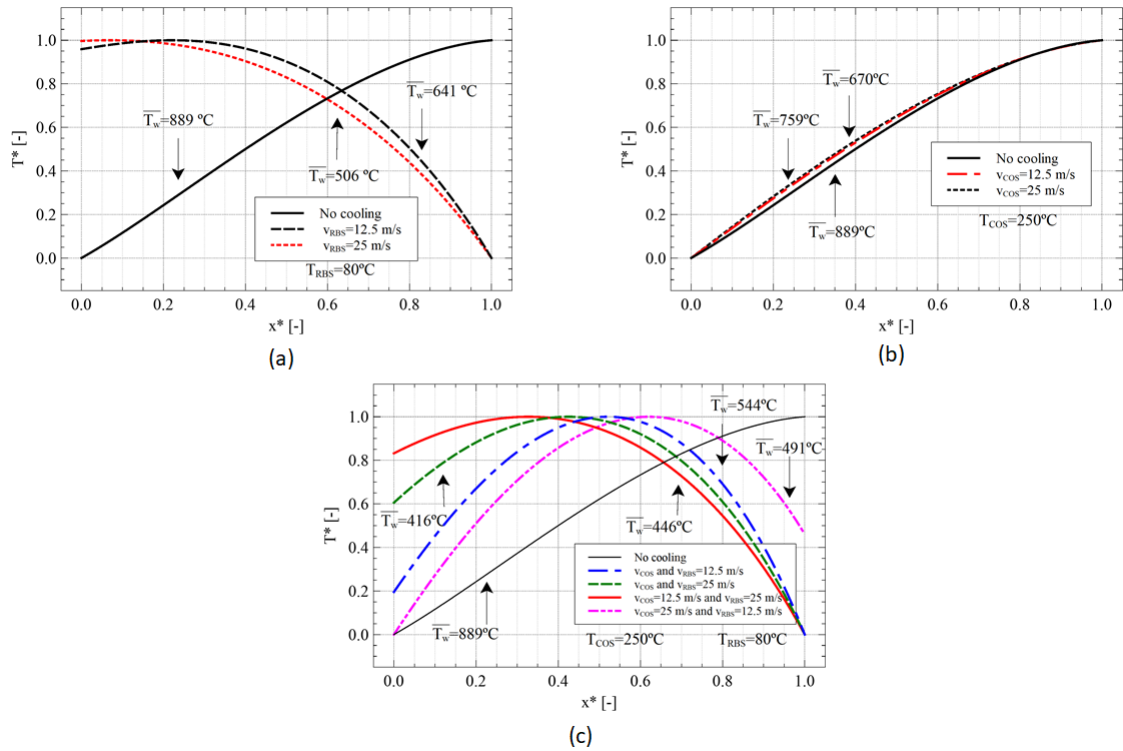


Figure 3.20: Dimensionless temperature profiles for cases with cooling inside RBS (a), COS (b), and RBS and COS (c).

3.2.8 Effect of cooling strategy

The numerical simulations provided information on the heat transfer associated to different cooling strategies defined in Section 3.1.3. A direct observation of the results of Figure 3.11 in Section 3.1.3, leads to the conclusion that the cooling strategy A removes more heat from the window since the average Nusselt number is higher for the same Reynolds number. This observation is proved with the implementation on the model and with the results of average window temperature in Table 3.9. The results are displayed for the nominal operating condition. The strategy B registers 40°C higher average window temperature than strategy A.

Table 3.9: Average window temperature as function of type cooling.

Cooling strategies	A	B	C
Avg window temperature, \bar{T}_w [$^\circ\text{C}$]	436.3	477.8	445.9

The average evaluation of heat transfer and window temperature can be limited. This means that strategy A could lead to higher thermal gradients along the window (removes more heat at the edge of the window than at the end) than cooling strategy B which removes heat on both sides, providing a more a symmetric field. The numerical simulations provided information on the average convection coefficient, but also locally. An example of the results of a numerical simulation for the same Reynolds with different strategies inside RBS is represented in Figure 3.21.

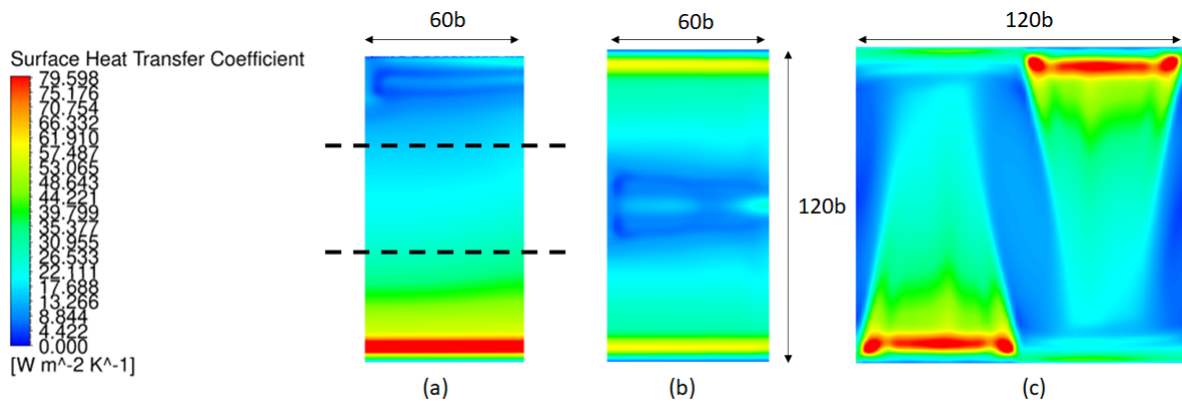


Figure 3.21: Local heat transfer coefficient at the window top surface (window-RBS interface) for different cooling schemes: (a) Scheme A; (b) Scheme B; and (c) Scheme C.

The regions with higher heat transfer convection coefficients match the zones near the injection due to the wall jet attachment. This region does not begin immediately at the edge due to backward-facing step that the wall jet faces. The region with lower heat transfer coefficient for strategy A is at the opposite wall as expected due to the reduced velocities on this region. This effect is less evident for strategy C since has an alternated scheme of cooling. Strategy C registers other region with lower heat transfer, at the middle of the window due to the effect of collision between opposite jets. The collision is not direct but affects the flow field and is responsible for the triangular shapes that can be observed. The situation of direct collision between jets is registered for strategy B. After the attachment, the jets start to develop until collide at the middle of the plate where the stagnation region registers very reduced velocities. The flow starts to develop on the normal direction and the effect observed is in accordance with literature [62, 63]. Cooling scheme B offers less variation of the convection coefficient (lower root mean square) by comparison with the other cooling strategies for all the Reynolds numbers considered.

The previous information of heat transfer is accounted by regions of interest (see dashed black lines in Figure 3.21(a)). Due to non significantly change of local heat transfer on longitudinal direction for strategies A and B, only 3 regions of interest were considered while for the strategy C, 9 regions of interest were considered due to the tri-dimensionality. The information is accounted in the 1D model and the results allow to develop not just an average window temperature for the entire window, but in different local regions. This is an assumption based on the low thermal conductivity of the window material and the local results for a nominal operating condition are displayed in Figure 3.22.

The results are qualitatively similar to the ones observed in Figure 3.21 since the cooling inside COS has a lower impact when compared with the cooling inside RBS. This means that if the cooling inside COS had a higher impact on reducing the temperature, the high temperatures should be registered at the opposite edge for cooling A.

The maximum window temperatures for cooling B and C are at the middle of the plate since the stagnation/collision region inside RBS is the same as COS. The collision in cooling scheme C is not so direct as the scheme B and therefore the temperatures are not so high.

For other strategies such as A, the region inside RBS which removes less heat due to reduced velocities matches the region inside COS which removes more heat.

Cooling strategy C registers a lower maximum of temperature and less gradient of temperature than the other strategies for the nominal operating condition.

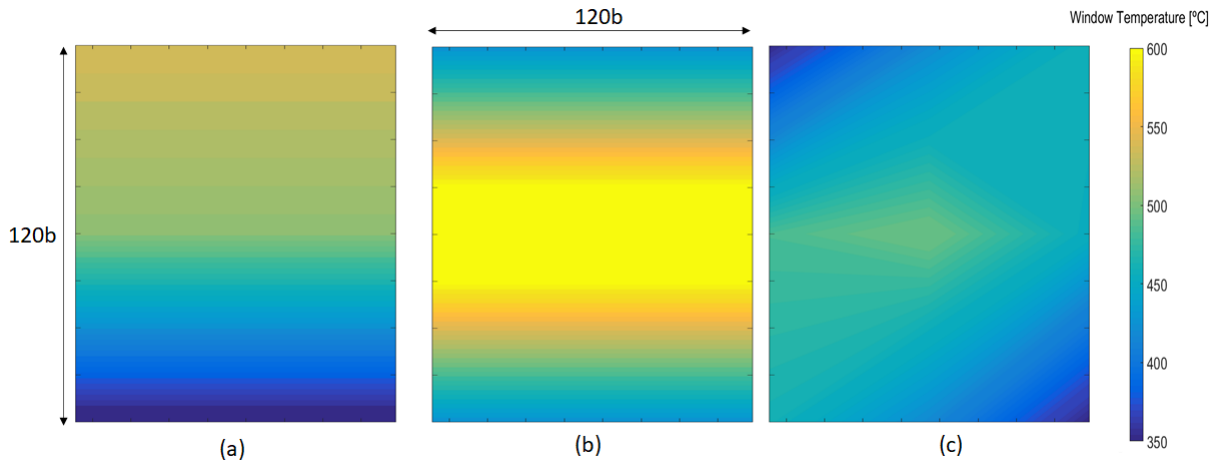


Figure 3.22: 2D window temperature for nominal operating condition and different cooling schemes: (a) Scheme A; (b) Scheme B; and (c) Scheme C.

3.2.9 Effect of burner’s advective output in cooling

Cooling inside RBS differs from COS since has an impingement jet (burners exhaust gas), normal to the window. The advective contribution of burner’s output has an impact on the wall jet heat transfer of the window and this impact differs depending on the operating condition of the burner. To analyze the effect of burners advective output on the window convective heat transfer behaviour, a constant flue gas temperature is considered along with different flue gas mass flow rates. Numerical simulations in the module of Figure 3.9 were performed in order to inspect the impact of burner’s power on the heat transfer by the wall. Two different scenarios were considered: nominal power and low power (7.5 times lower). The correlations are now different and the results for cooling strategy A inside RBS are displayed graphically in Figure 3.23.

The results show that for the same Reynolds numbers as the power is reduced, the heat transfer from the window is increased (Higher Nusselt number for low burner’s power). This effect is expected but is very reduced. The Nusselt number registers differences of around 3%. The implementation on the 1D window model for the situation with cooling only in RBS shows a lower temperature of the window for the low power situation (479°C/492°C- average window temperature for low/high burner’s power).

The studies on heat transfer with cross flow effects usually demonstrate a higher impact in flow field and heat transfer [64–66]. This study does not demonstrate that effects since registers a very reduced ratio of velocities between wall jet and burner’s output (cross-flow) which justifies the reduced difference. The analysis of the flow field on a further chapter will also show that the interaction between wall jet and burner’s output is after the jet reaches the opposite wall and near the extraction port. The wall jet

removes heat from the window, acting as a "curtain". This effect was analyzed to other cooling strategies and similar results were observed.

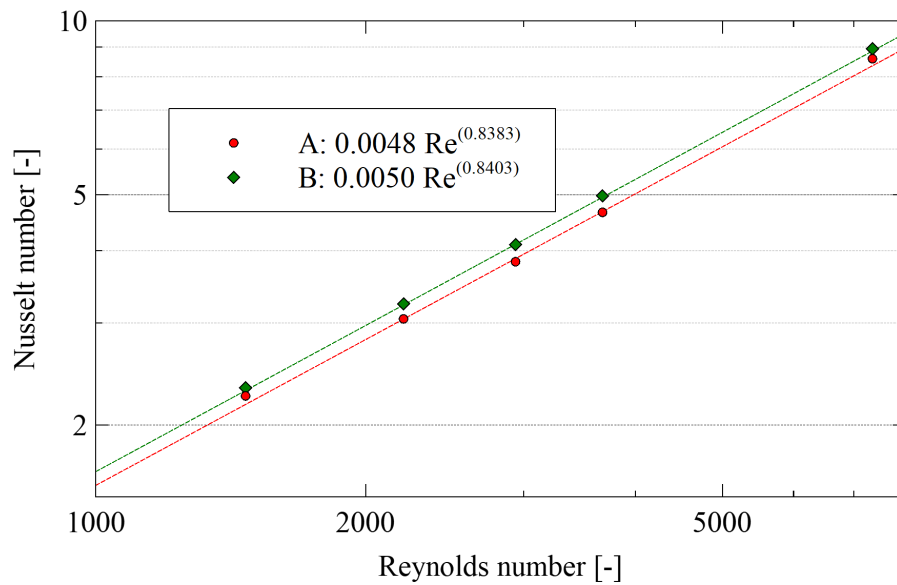


Figure 3.23: Nusselt number correlation for nominal power and 13% nominal power.

3.2.10 Effect of cooling gas injection angle

An investigation on the cooling gas injection angle (β) was performed on the numerical simulations. This angle is defined as the angle between normal direction of cooling with the window plane (see Figure 3.24).

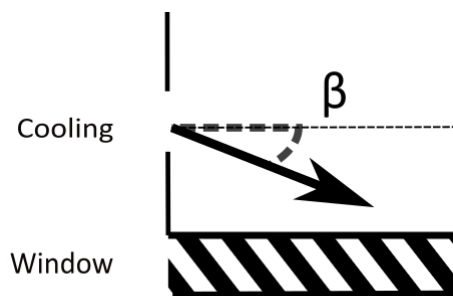


Figure 3.24: Schematic representation of cooling gas injection angle (β).

Different numerical simulations were performed and the results of local convection coefficient considering three different injection angles are presented in Figure 3.25. The results are referred to a case of cooling inside COS at a reduced velocity for strategy A. The results are only displayed on the attachment region since there is no difference on the region after $x/b = 20$.

The peak of local convection coefficient corresponds to the local where the wall jet is attached to the wall. Considering an injection with an angle and not entirely parallel to the window, the attachment to

the window (peak) is closer to the edge ($x/b = 0$). The magnitude of this maximum is also slightly higher for cases with higher angle since there is less loss of heat. The injection of a cold wall jet with an angle bring negligible differences in terms of total heat removed from the window (similar average convection coefficient) since the region of study is up to $x/b = 120$.

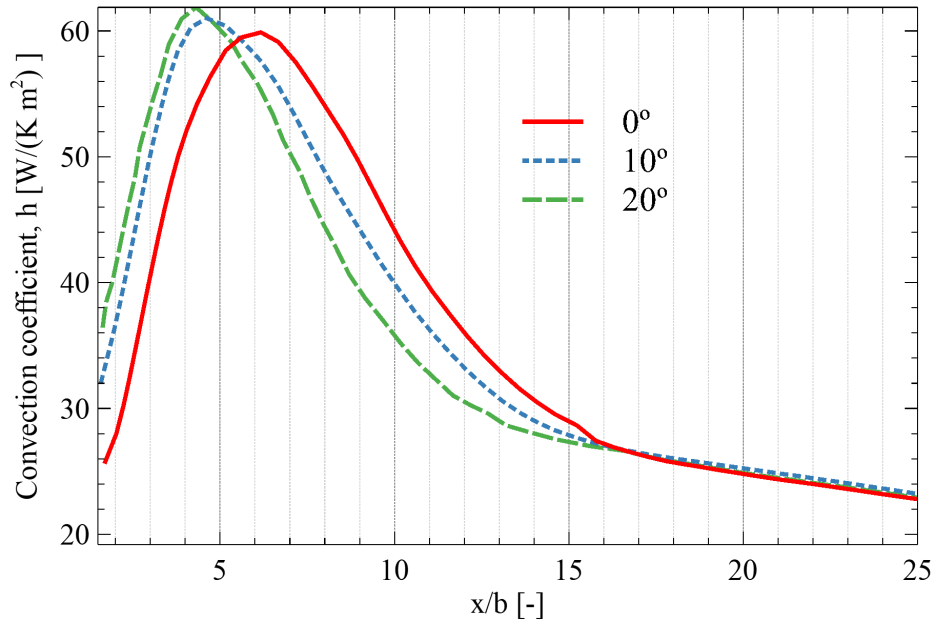


Figure 3.25: Local convection coefficient for numerical simulations with a different angle of injection.

3.3 Energetic optimization

This section intends to dictate the optimal situation of cooling. The optimal situation matches the proper functioning at the reduced energy cost.

3.3.1 Objective function

The optimization technique is focused on finding the optimal solution and defining the objective function is crucial for this purpose. The system needs to comply with the safety of the operation at optimal conditions, at the low possible cost (minimum of the function).

The objective of the optimization is not minimize the temperature of the medium but to find the minimum cost of energy to comply with a stable and safe operation.

The lowest cost possible is observed when there is no need for an additional strategy for reducing the window temperature (cooling) since the system is already in full compliance with the objective. However, there are operating conditions for which the system performance (window thermal performance) does not comply with the requirements — the window temperature becomes higher that a critical value — and an optimized active window cooling conditions should be evaluated and applied.

Figure 3.26 represents schematically the environment and the relevant energy fluxes. The energetic cost of the cooling operation is the thermal power of the outside HX ($Q_{HX,RBS} + Q_{HX,COS}$). The fluid

extracted from the furnace internal environment (RBS or COS) passes through an HX and is injected again into the environment. HX (additional strategy) represents the cost of this additional operation and the objective function is based on this device.

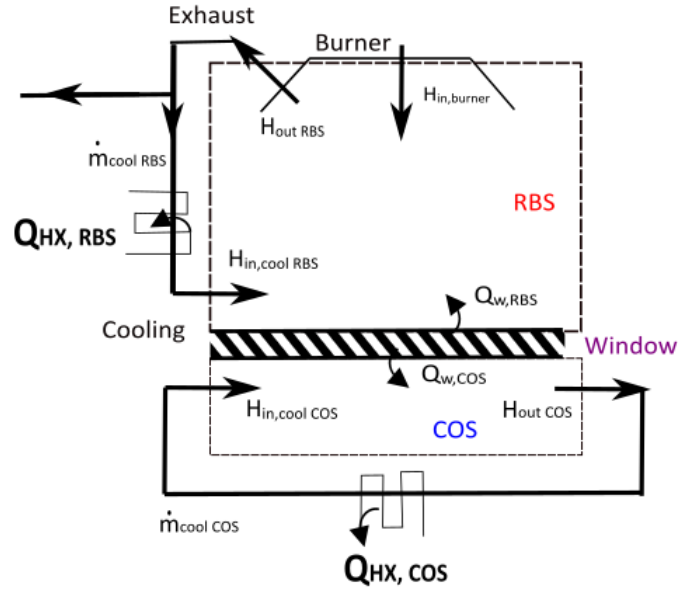


Figure 3.26: Schematic representation of HX situations in both sections.

The HX removes part of the extracted fluid heat, according with a mass flow rate ($\dot{m}_{coolRBS}$ and $\dot{m}_{coolCOS}$) and a cooling inlet temperature. The lowest possible cost of the system is then defined as the lowest heat transfer removed by the HX:

$$Q_{HX,RBS} = \dot{m}_{coolRBS} \times (h_{outRBS} - h_{in,coolRBS}) \quad (3.28a)$$

$$Q_{HX,COS} = \dot{m}_{coolCOS} \times (h_{outCOS} - h_{in,coolCOS}) \quad (3.28b)$$

The minimization of this function leads to minimize the mass flow rate to the lowest possible and minimize the difference of specific enthalpy between extracted and injected (h_{out} and $h_{in,cool}$). The function is only completely defined for optimization when the function becomes only function of the optimized variables, which are the operating conditions of cooling. The total enthalpy of extracted fluid from environment (H_{outRBS} and H_{outCOS}) is dependent on the energy balance performed to the system (dashed lines in Figure 3.26). The difference of total enthalpy is equal to the heat removed from the window and gained by the system:

$$H_{outRBS} - H_{in,coolRBS} - H_{in,burner} = Q_{w,RBS} \quad (3.29a)$$

$$H_{outCOS} - H_{in,coolCOS} = Q_{w,COS} \quad (3.29b)$$

The thermal power removed to window by convection is computed based on the 1D model developed

and the variables are dependent on cooling conditions:

$$Q_{w,RBS} = A_w \times h_{RBS} \times (T_w - T_{RBS}) \quad (3.30a)$$

$$Q_{w,COS} = A_w \times h_{COS} \times (T_w - T_{COS}) \quad (3.30b)$$

The objective function is already completely defined according with the operating conditions of cooling.

3.3.2 Optimized variables and constraints

The variables to optimize correspond to the cooling gas injection velocity and temperature for the RBS (v_{RBS} and T_{RBS}) and COS (v_{COS} and T_{COS}) and the cooling strategy (five variables). Cooling gas injection velocities and temperatures are continuous variables along the corresponding domains while the cooling strategy considers three discrete schemes (Scheme A, B, and C — see Figure 1.2).

The optimized continuous variables are constrained in a domain with lower and upper bounds:

- $250^\circ C < T_{COS} < 450^\circ C$
- $5\text{m/s} < v_{COS} < 25\text{m/s}$
- $80^\circ C < T_{RBS} < 450^\circ C$
- $5\text{m/s} < v_{RBS} < 25\text{m/s}$

The atmosphere inside COS is loaded with solvent and due to condensation problems for temperatures below $250^\circ C$, that was considered the lower limit of cooling gas temperature (T_{COS}). The lower limit of cooling gas temperature inside RBS is defined according with industrial constraints. The lower limits of velocity were defined due to the Reynolds limits of the study conducted in Section 3.1.3 and the maximum limits were defined according with industrial constraints.

The optimal solution is not exclusively constrained by the provided solution space (domain limits for each optimized variable). The optimal solution is also constrained by a maximum temperature and a maximum temperature gradient that must be below the corresponding critical values:

- $T_{max,w} < T_{critical}$
- $\Delta T_w < \Delta T_{critical}$

The variables ($T_{max,w}$ and ΔT_w) are non-linear and depend only of the optimised variables according with the 1D model developed.

3.3.3 Results

The optimization toolbox of MATLAB was used to solve the optimization formulation previously presented. The solver method used was the initial-point algorithm and a search with multiple initial points (10) is used to dissipate the errors. The genetic algorithm resulted in a high computational effort due to a non-linear constrained based on the model developed.

The response to the user is defined and the results are listed in Table 3.10. The results show that decreasing the critical temperature (first column), the demand for more cooling power increases (last column). The increase of this value is not entirely linear. To high maximum temperatures between 800°C and 600°C, the cooling goes to the low limits of cooling inside RBS (maximum temperature and lowest velocity). For higher critical temperatures (800°C to 600°C), the system makes use of the HX inside COS. The strategy starts to fix the maximum temperature inside COS (T_{COS}) and increasing the velocity (v_{COS}) to meet the requirement (800°C and 750°C). Afterwards, when the maximum velocity is attained, the strategy dictates a reduction of the inlet temperature temperature (T_{COS}) as shown from 700°C to 600°C. The cooling scheme continues to register the maximum temperatures at the middle of the window, region of interaction between opposite jets.

The maximum limits of cooling inside COS are achieved (T_{COS} equal to 250°C and v_{COS} equal to 25 m/s) when there is a need of a maximum temperature below 600°C. The system demands then cooling power inside RBS. While the cooling power increased 6 kW to reduce the maximum temperature from 800°C to 600°C degrees, to reduce from 600°C to 550°C, the system demanded more 30.5 kW. The flow which is removed of RBS is mixed with the burners output as can be observed by the Figure 3.26 and registers a high enthalpy when compared with the case inside COS.

The optimal response dictates a reduction of the injection temperature (T_{RBS}) to the minimum possible and an adjustment on the velocity (v_{RBS}) to meet the requirements.

The optimal solution dictates the optimal scheme as the scheme A when the maximum temperature is very high at the middle of the plate. After a certain maximum temperature, the system dictates that the optimal solution is obtained with scheme C. The change from Scheme A to C as the critical temperature is decreased is observed since increasing the cooling power inside COS leads to maximum temperatures on the opposite edge and not at the middle for scheme A. This effect is not registered in cooling scheme C. The maximum temperatures keep at the middle of the window, region of interaction between opposite jets.

There is an increase of the temperature gradient inside the window as the maximum temperature is reduced until the cooling inside RBS starts to reduce the injection temperature and increase the velocity (critical below 550°C). The gradient of temperature is reduced afterwards.

Scheme A predicts a lower temperature gradient for cases with high maximum temperature requirement. Completing a simulation similar to the table, with a maximum temperature equal to 750°C and a gradient of temperature lower than 100°C, the system will dictate the optimal choice as the scheme A.

Scheme B (two sided cooling) does not become an optimal choice in any conditions due to the stagnation region at the middle of the window on both regions, above and underneath which cause a high maximum and high gradient of temperature.

For critical temperatures below 400°C, the system dictates that the operation is not feasible.

Table 3.10: Window cooling optimization results.

Requirement		Optimised variables				Objective function	
$T_{critical}$	ΔT_w	T_{RBS} [°C]	v_{RBS} [m/s]	T_{COS} [°C]	v_{COS} [m/s]	Scheme	Power [kW]
800	62	327	5.0	427	10.2	A	28.9
750	133	327	5.0	427	21.7	C	30.7
700	140	327	5.0	384	25.0	C	32.0
650	152	327	5.0	319	25.0	C	33.3
600	159	327	5.0	265	25.0	C	34.5
550	143	80	5.5	250	25.0	C	65.0
500	129	80	11.6	250	25.0	C	110.9
450	115	80	18.6	250	25.0	C	153.0
400				Not feasible			

3.4 Chapter conclusions

The parametric studies and the optimization investigation on the window thermal performance provided the following conclusions:

- The situation without cooling registers a very high temperature inside the glass window - 889°C. The increase of the glass thickness leads to an logarithmic increase of the temperature inside the window and windows with higher absorption coefficient absorb more energy and therefore register higher temperatures inside. For the same burner power, burner's radiative efficiency has a strong impact on the temperature of the window due to the high temperatures of the burner surface and coil temperature has a negligible effect due to the reduced temperature and emissivity;
- Cooling is a very influencing factor to reduce the window temperature, specially inside RBS. Cooling inside RBS has a higher impact than cooling inside COS due to reduced injection temperature and higher mass flow rate. The wall jet removes heat from the window, acting as a "curtain". The burner's output has negligible effect due to the reduced velocity ratio. The injection of a cold wall jet with an angle brings negligible differences in terms of heat removed from the window for the case studied.
- Different cooling strategies lead to different temperature profiles along the entire plate and demand a local evaluation. The nominal case was evaluated and an alternated cooling scheme provides a lower gradient of temperature, with the maximum temperature lower than the other schemes- $T_{max} = 505^{\circ}\text{C}$.
- Cooling from one-side (scheme A) removes more heat from the window, leading to reduced average window temperature ($T_w = 436.3^{\circ}\text{C}$). Alternated cooling scheme (scheme C) registers slight higher temperatures - $T_w = 446.5^{\circ}\text{C}$.

- Cooling from two-sides (scheme B) leads to less heat removed to the window and higher gradient of temperature due to the stagnation region at the middle of the plate.
- The optimization procedure leads to a direct response to the user of the optimal conditions of cooling. The cooling power demand increases when there is a need of a lower maximum temperature.
- The optimization shows that the use of the HX inside COS is more relevant in energetic purposes since there is no mixing with an hot fluid from the burner's output.
- The choice of the best cooling scheme is not universal because it depends on project requirements. Cooling from one side (scheme A) is more efficient than alternated cooling scheme (scheme C) when the user does not demand lower window temperature. The minimum temperature gradient is registered at high window temperatures.

Chapter 4

3D numerical simulations of the curing oven

This chapter is devoted to the modeling and simulation of the full curing furnace. The 1D model developed offers the optimal response to the user on the thermal control of the window but has limitations and assumptions. The 1D model does not consider the enclosure walls of the curing furnace and the model is based on assumptions which do not consider the interaction between different burner's emitting radiation surfaces. The model also does not simulate the flow field and heat transfer inside RBS and COS coupled with the glass partition. The numerical simulations of the full curing furnace will study this effects.

An initial section intends to describe the simulation details of the entire furnace (Section 4.1). The following section is focused on the analysis of the window thermal performance (Section 4.2). The energy balances are verified and analysed (Section 4.3). A comparison of the results with the 1D model is performed (Section 4.4) and the conclusions drawn (Section 4.5).

4.1 Geometrical and modeling details

The curing furnace as already described in introduction is composed by two coupled modules (RBS and COS). The RBS is composed by four sets (batteries) of burners. Each battery of burners is composed by two rows of four individual burner units flanked by flue gas extraction slots. The four batteries of burners are at the coil entrance side.

The gas inside COS is removed on bottom by an extraction port at middle (green arrow on bottom of Figure 4.1). The outlet of the recirculation inside COS is at the end of the curing oven section - observed by the green line in Figure 4.1.

The insulating walls around the oven components consist of a 200 mm thick insulation layer sandwiched between two austenitic and heat resistant steel sheets with 1 mm thick each.

The separation of the two sections (RBS and COS) is made by a window, which allows the radiative exchange to solvent evaporation. For the zone which is not underneath the burners, there is a region

which is not transparent and do not participates in radiation since it is opaque.

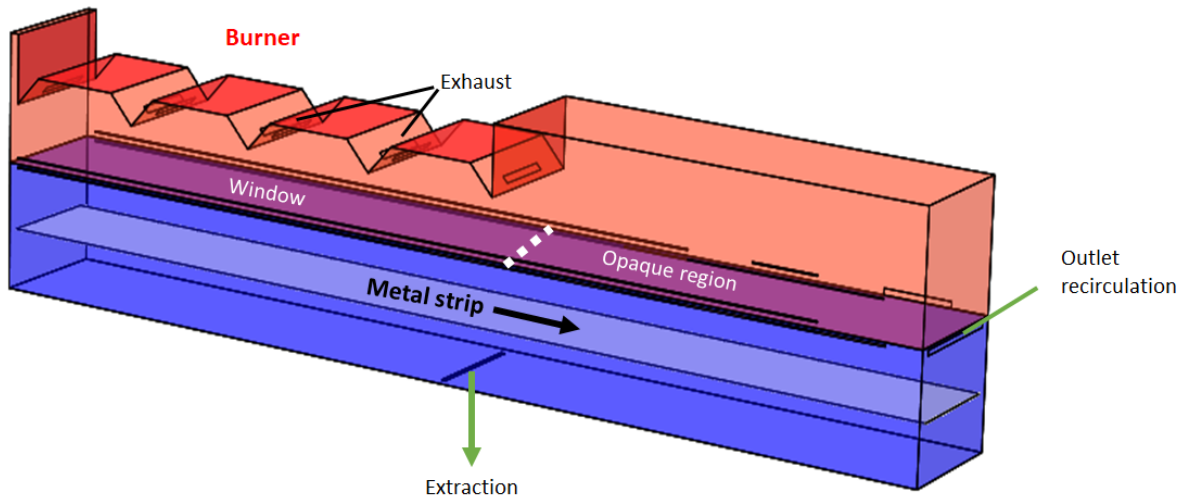


Figure 4.1: 3D model of the full curing furnace.

A commercial software (ANSYS Fluent) was used to discretize the physical domain and to solve the set of 3D governing equations for mass, momentum, and energy conservation in steady-state form and also the chemical species transport equation for O_2 , CO_2 , H_2O , N_2 and an effective solvent species (see Section 2.1). Since the fluid has several species involved, the fluid was defined as a gas mixture. The fluid mixture is modeled according to the mixture average formalism. The apparent molecular and thermophysical properties for the effective solvent species were evaluated taking into account the detailed composition of the solvent mixture. The properties related to species were defined according with Fluent database, considering temperature dependence with Sutherland's law. The ideal gas model was considered for the evaluation of the fluid density. The $k - \epsilon$ turbulence model was applied to provide closure for RANS equations. In addition, the radiative heat transfer exchanges in the full 3D domain were taken into account. The radiative heat transfer contribution to the energy balance equations of gas and solid regions was considered through the application of the DOM with an S6 angular discretisation. The gas is considered as non-participant to radiative heat transfer due to the reduced mass fraction of participant gases to radiation (CO_2 and H_2O) but the glass material that separates both oven regions (RBS and COS) is considered as a participating medium – the glass material simultaneously absorbs and emits radiation.

The 3D computational domain was discretized considering hexahedron cells. The choice of the type of mesh was due to the model geometry following the three perpendicular directions as the axes. The directions of the injected fluid streams are mainly aligned with the axes, therefore the option of with hexahedron cells will decrease the numerical false diffusion and achieve an enhanced solution accuracy. This discretization has a very important role, not only in terms of accuracy, but also, in terms of computational effort to achievement of a convergent solution. The refinement and low-Re modeling near the window was not possible due to the unaffordable computational cost. The numerical model resulted in a mesh of 6.18 million cells in total.

4.1.1 Operating and boundary conditions

The numerical simulations are conducted for a nominal operating condition of 600 kW with the three first batteries of burners active. At the burner's outlet section, temperature and velocity values are prescribed for the flue gas stream (2 m/s at 1340 K – advective contribution – and a fixed temperature value (1400°C) is applied on the corresponding surface area – radiative contribution. The surface temperature was estimated since it is not possible to impose a radiative flux. The molar composition of the flue gas is equal to already defined in Section 3.1.3. Similar boundary conditions are considered for the cooling gas injection sections. The injection of the flue gas in RBS was simulated with a temperature imposed and a velocity associated (25 m/s at 80°C). A pressure-outlet boundary condition stating atmospheric pressure conditions was applied at the flue gas extraction sections.

The nominal operating condition corresponds to a solvent evaporation of 30.3 L/h, with a metal strip velocity equal to 0.5 m/s. The boundary conditions related to the solvent species evaporation were prescribed as an uniform mass source along the metal strip inside the COS (7.5×10^{-3} kg/s). The metal strip temperature is prescribed with a linear increase inside the COS from 25°C to 250°C.

Inside the curing oven section, two sub-systems are present. The extraction system – which aims to collect the solvent species evaporated – is at the bottom of the COS and it was defined with a specific mass flow rate leaving the furnace (0.0928 kg/s). After solution converged, this value of mass flow rate was verified and was in accordance with the target value. The other system is the recirculation system that recirculates the flow inside the COS and cools the window from underneath. It was defined as a recirculation boundary condition with an inlet temperature of 250°C (minimum) and a mass flow equal to 0.0852 kg/s - which corresponds to a velocity inlet equal to 12.5 m/s.

The enclosure walls were defined as opaque surfaces with an emissivity equal to 0.8 – value consistent with the material of the inner sheet. The walls were also considered as adiabatic due to the constituent materials.

4.2 Glass thermal analysis

The glass is the focus of the analysis and different situations are analyzed in this section: without cooling (Section 4.2.1) and with the remove of heat by cooling injection underneath and above (Sections 4.2.2 and 4.2.3, respectively).

4.2.1 Without cooling

The situation without any cooling system applied underneath and above the window is herein analyzed. The incident radiation (irradiation) on the upper surface of the glass is presented in Figure 4.2(a). The high values are at the center, below the first and second row of batteries as expected. The temperature distribution shows very high temperatures underneath the active burners, see Figure 4.2(b). The average temperature of the window is 926°C and the distinction between the two distribution is due to the convective heat exchange between gas and window.

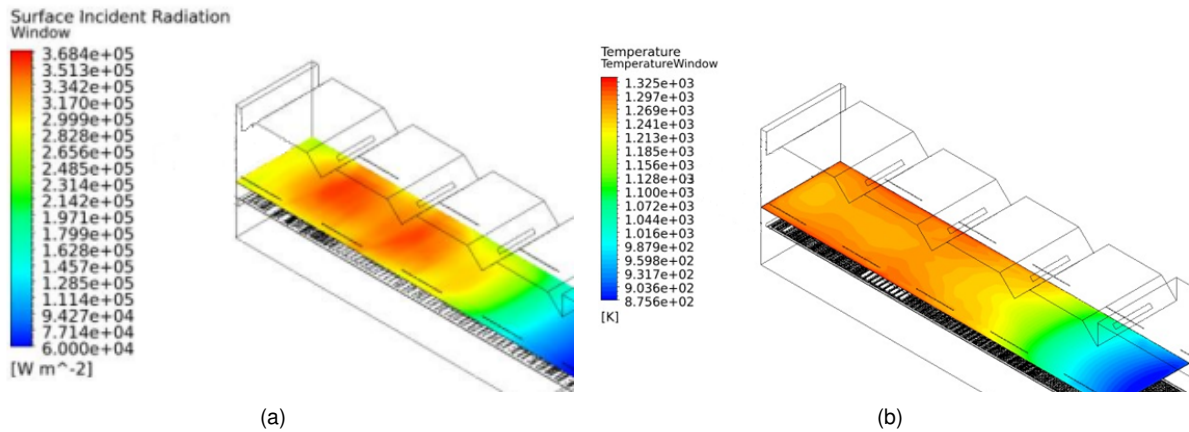


Figure 4.2: 2D contour on top surface of the window for the situation without cooling for: (a) incident radiation; and (b) temperature.

4.2.2 Cooling inside COS

This investigation is conducted with the system of cooling applied below the burner in an alternated cooling scheme (cooling scheme C - black arrows in Figure 1.2(c)). The cooling is applied with a step height 3 times higher than the jet height (15 and 5 mm, respectively). Figure 4.3 depicts the velocity streamlines inside the COS for the transversal alternated recirculation flow. The flow pattern removes heat from the window in a triangular shape due to the influence of the opposite flow, which results in a temperature distribution as the one presented in Figure 4.4. The hotter regions are at the opposite side of the injection and at the center, between the collision between those jets. This effect is in agreement with previous results for the convection heat transfer coefficient (Figure 3.21).

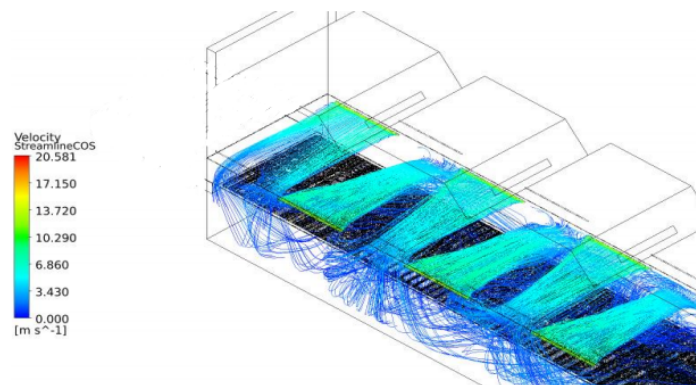


Figure 4.3: Velocity streamlines for recirculation flow with cooling strategy C.

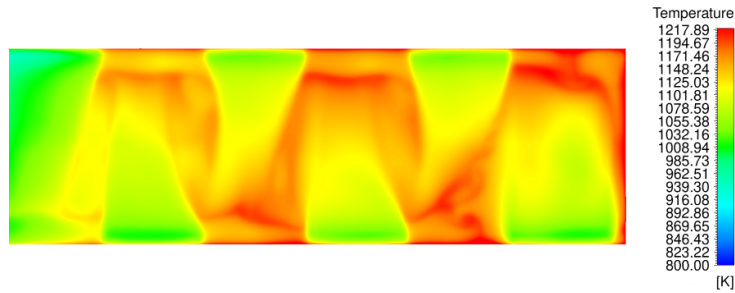


Figure 4.4: Window temperature distribution for recirculation flow with cooling strategy C.

4.2.3 Cooling inside RBS

This section analyses the thermal performance of the window according with certain conditions of cooling inside RBS (cooling scheme, cooling slot position and mass flow rate).

Effect of cooling scheme

A direct comparison between two different schemes of cooling inside RBS is performed. The numerical simulations of this study have small differences when compared with the geometrical model presented in Section 4.1. The numerical simulations also do not include the effects of cooling inside COS - underneath the window. The two schemes considered on this comparison are the one-sided cooling and the alternated (cooling scheme A and C - see red arrows in Figures 1.2(a) and (c)). The temperature distributions inside the window for the two different cases are presented in Figures 4.5(a) and (b).

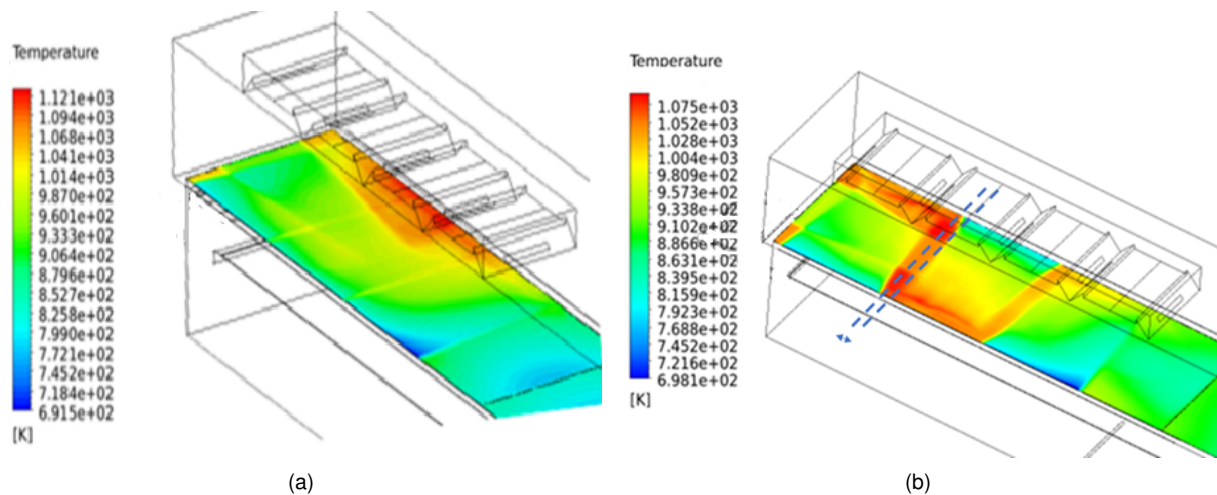


Figure 4.5: Temperature contour for different cooling schemes inside RBS: (a) One-sided - Cooling scheme A; and (b) Alternated - Cooling scheme C.

The wall jet does not face a step at the entrance and therefore the lower temperatures are observed at the edge of the cooling slots. The hotter regions are observed on the opposite region, especially on the region of the second battery of burner where the incident radiation is higher. The distribution of the window temperature is different for the alternated cooling scheme. The hottest zones are registered on the opposite side of the cooling jets and in the middle zones between them (see Figure 4.5(b)).

Due to the tri-dimensionality, the opposite jets have an impact on each other, reducing the velocity, and consequently, the heat removed from the window. This effect is increased by the distance between the cooling inlets. Where a cooling inlet ends there is a distance until the start of the next cooling inlet on the other side – see the blue dashed lines in Figure 4.5(b). The results show a negligible difference between both cases in terms of average window temperature, which is in agreement with the the results of the previous study (see Section 3.2.8).

Effect of cooling slot position

The alternated cooling (cooling scheme C) inside RBS varies the side of cooling injection. The relative position between cooling inlets and the extraction system is here studied. Two numerical simulations were performed in accordance with the numerical model described in Section 4.1. The only differences between both simulations is the relative position of cooling injection. The first model has 7 cooling slots along the burner’s output and the second simulation has 6 cooling slots which are perfect aligned with burner’s output (see black and red dashed lines in Figure 4.6).

Figure 4.6 shows the temperature field inside RBS. The analysis of the environment is a very important step to understand the root causes of the differences regarding the thermal performance. For the simulation without alignment, there is cooling flow going directly towards the exhaust system (blue circle in Figure 4.6(a)). The non attachment of part of cooling is also verified for the case where the cooling slots are aligned but the flow does not go direct to the extraction (blue circle in Figure 4.6(b)). The average temperature inside the window is reduced 43°C by the alignment of cooling injections with burner’s output (716°C to 673°C).

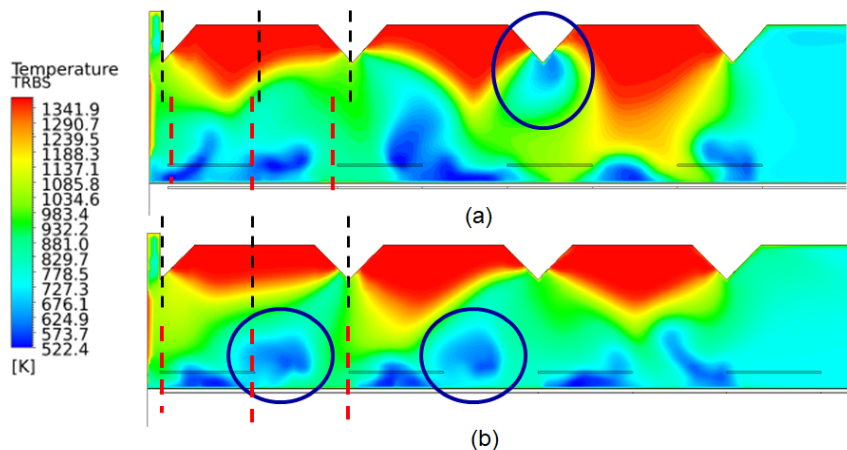


Figure 4.6: 2D contour plot in a longitudinal plane for two different situations: (a) without alignment; and (b) with alignment.

Effect of mass flow rate

The following study focus on the impact of the mass flow rate of cooling inside RBS. The study is performed with the furnace model which has the cooling gas injection sections not aligned with the

batteries of burners. Figure 4.7 presents the longitudinal window temperature profile at middle plane for different cooling gas injection velocities: 0 m/s (without cooling), 25 m/s, and 50 m/s.

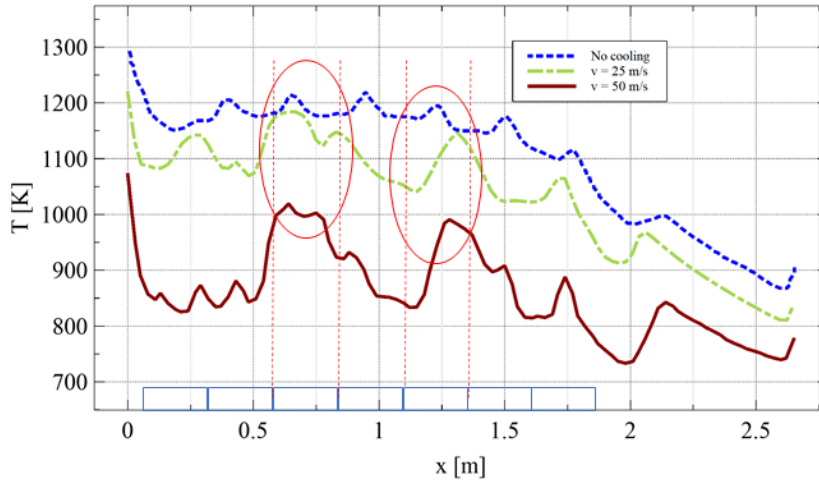


Figure 4.7: Window longitudinal temperature profile for different cooling gas mass flow rates.

As expected, a higher cooling mass flow rate corresponds to lower window temperatures. The hot regions keep the location on both cases (see red circles and peaks in Figure 4.7). The reduction of temperature is less effective on the hot regions. The results indicate that the cooling has not the same efficiency along the plate. Making a match with the cooling inlets (see the blue rectangles in Figure 4.7), the hotter regions match the second and third cooling gas injection slots from one side and with the zones underneath the extraction systems.

4.2.4 Combined cooling

The following study is performed with the systems of cooling applied inside RBS and COS.

Figure 4.8 shows the window temperature distribution for the current situation. The distribution of temperatures is not uniform in any direction and there is a significant difference between cooler and hotter zones. The injection direction of cooling gas applied above the window is in accordance with the blue arrows. The zones which register the higher temperatures match the zones near the cooling injection from only one side (bottom side of Figure 4.8).

Figures 4.9(a) and (b) show the streamlines with origin at the cooling gas injection section from one side, demonstrating the behaviour of the cold wall jet flow. The cooling gas flow is attached to the window until reaches the opposite wall, the stagnation point. The flow starts to grow on the opposite wall, in y direction. The interaction with the flow coming from burners is only afterwards, near the extraction port and burner's output. The flow creates a spiral movement across the longitudinal distance, where it follows the path to the extraction systems. The cooling applied faces a step at the injection which is 10 times higher than the jet height ($10b = 50$ mm).

Figures 4.10 (a) and (b) show streamlines with the corresponding velocity magnitude (left figures) and temperature (right figures) at the transversal cross-sections $x = 256$ mm and $x = 456$ mm respectively.

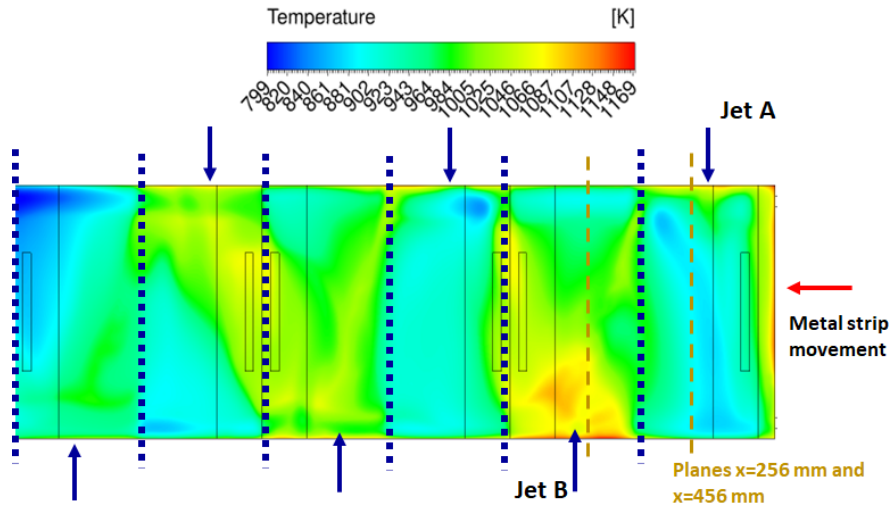


Figure 4.8: Window temperature distribution with combined cooling.

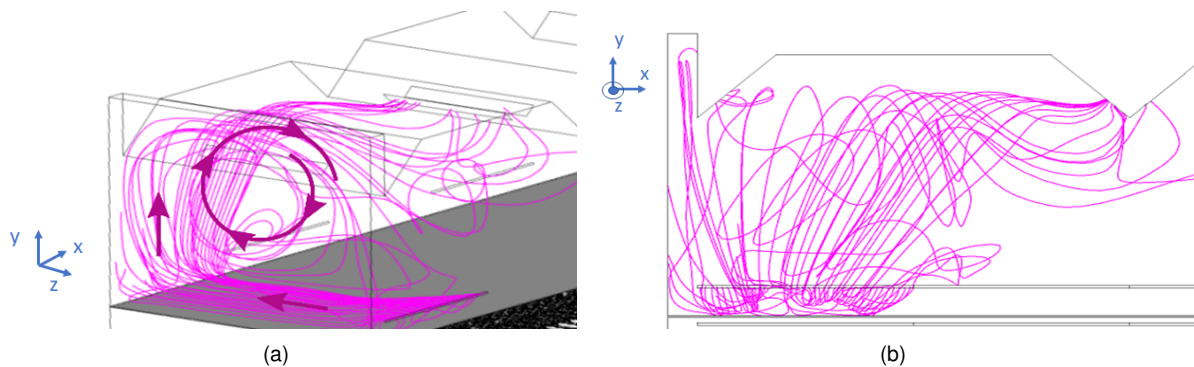


Figure 4.9: Streamlines with origin at cooling; (a) Iso-view; and (b) XY view.

The planes are at a distance equal to 100 mm from the centre of the first battery of burners - see the brown dashed lines in Figure 4.8. Figures 4.10(a) represent the cooling behaviour of Jet A — see the location of Jet A in Figure 4.8. Jet A is identified by the highest velocities and the lowest temperatures. The wall jet faces a step and then attach to the window, after the stagnation region. The movement on the opposite wall and the spiral movement due to the interaction with the burner is possible to identify as well. For Jet B (see its location in Figure 4.8), Figure 4.10(b) should show a symmetric behaviour as Jet A, but that is not observed. Jet B (blue arrows) does not attach to the wall. This effect results in the temperature distribution observed, with the hot regions on this zone. The flow does not achieve the burners' output in a same way as Jet A and therefore the spiral created is very reduced compared with the one created from Jet A. The longitudinal movement of the spiral is proved by the spirals from Jet A appearing in the other plane and vice-versa.

The analysis of the cooling flow inside RBS show ineffectiveness from part of cooling. The root cause for that effect is the high step height, which is 3 times higher than the cooling inside COS and 10 times higher than the jet height. The high step height causes the non-attachment to the window. The inefficiency is also evident due to the dominant side created by the wall associated to the three-dimensionality. This means, that jet A has a wall next to the injection which forces the cooling on x

direction, making it harder the attachment by jet B. This effect explains the remaining flow pattern inside RBS.

The adiabatic walls have a radiative gain that results in a loss by convection to the fluid. The walls are at very high temperature and therefore the surrounding fluid registers higher temperatures as can be observed by the temperature contours.

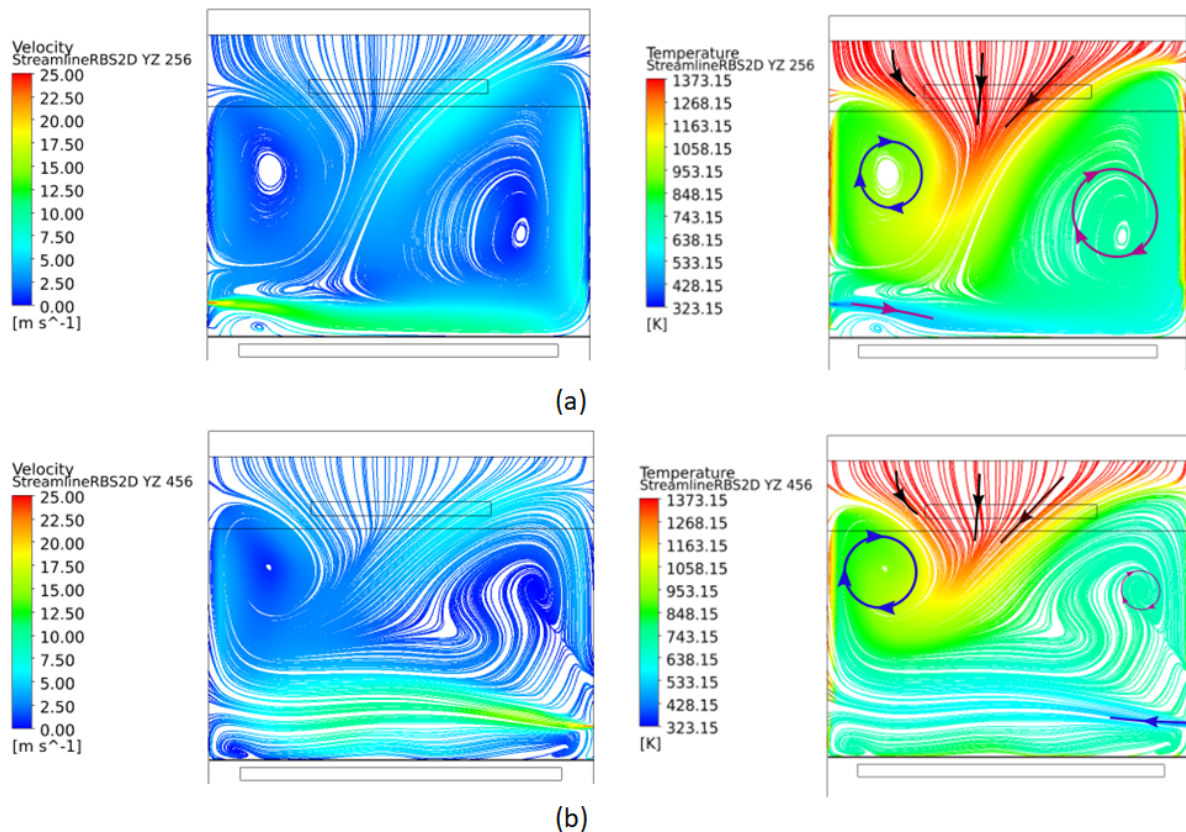


Figure 4.10: Streamlines of velocity (left) and temperature (right) at two different transversal cross-sections: (a) $x=256$ mm; and (b) $x=456$ mm.

4.3 Energy balances

The nominal operating condition corresponds to a total power output of 600 kW. The radiative flux is not imposed and the value computed is around 181.60 kW, which is in agreement with the radiative efficiency equal to 0.3. The radiative flux from burners' output is not entirely directed towards the COS. The walls inside RBS have a radiative gain corresponding to 35.9 kW (19.74%) and the window absorbs 23.4 kW (12.86%). The inlet (cooling) and outlet (exhaust) sections have a radiative gain corresponding to 5.7 kW (3.14%). The remaining part of the radiative flux is transferred to the COS and absorbed by the coil. The coils absorbs 103.6 kW (57%) of radiative energy which complies with the requirements to drive the coating process.

The fluid mixture circulating inside the RBS is exchanging energy inside the system. An energy

balance to the fluid is performed in order to understand the enthalpy of the fluid which is extracted. Other advantage is guaranteeing the reliability of the simulation by matching and respecting the energy balance. The energy associated to the fluid entering and leaving was computed based on the mass flow and specific enthalpy of each computational cell (46.9 kW). This gain of energy should match with the heat exchange from the walls (35.9 kW) and window (11.5 kW) to the fluid, as it does.

4.3.1 Relevance of wall heat losses

The importance of wall heat losses through the furnace walls is investigated considering the wall insulation material and thickness. The investigation compares the overall performance for different thicknesses with the adiabatic case. An overall heat transfer coefficient was calculated and then implemented in the simulation. The overall heat transfer coefficient (U_{wall}) was calculated assuming one-dimensional conduction in cartesian coordinates with the geometrical parameters and thermophysical properties of the composite oven wall (2 steel plates of 1 mm and insulation material with thermal conductivity equal to 0.184 W/mK) and considering the external (surrounding) environment with a convection heat transfer coefficient (h_{ext}) equal to 20 W/m²K (natural convection range):

$$U_{wall} = \frac{1}{\frac{1}{h_{ext}} + 2 \times \frac{1mm}{k_{plate}} + \frac{t}{k_{insul}}} \quad (4.1)$$

This strategy represents a negligible computational cost to incorporate the wall heat losses since the addition of cells inside the wall is not required. Different cases were studied according to the thickness of the insulation material (t). The results are provided in Table 4.1.

The difference by considering the thickness of the insulation material leads to losses through them. The heat losses reduce in a proportional way with the increase of the thickness. The losses correspond to 1% of the total power input from the burners for the more realistic situation – $t=200$ mm. The major heat loss contribution is due to the walls of RBS (4.3 kW) since these walls are at higher temperatures compared to the walls of COS. This heat loss on the system also leads to a reduced temperature of the walls. The temperature difference is not significant since the losses are reduced. The effect on RBS environment is neglectable as the variation of the average temperature inside shows. The insulation material considered for the walls leads to reduced losses to the environment (1% for the realistic case) and therefore the system is almost adiabatic.

Table 4.1: Effect of furnace insulation wall thickness (mineral wall) on the furnace heat losses, furnace walls, and RBS (average fluid).

Insulation thickness, t [mm]	Losses [kW]	Walls Temperature [K]	RBS Temperature [K]
100	13.3	980	840
200	7.0	984	840
400	3.7	1002	840
∞ (Adiabatic)	0.0	1004	840

4.4 Comparison between the 3D furnace and 1D window model results

The analysis of the full furnace allows a comparison with the results obtained with the 1D model developed. Table 4.2 presents the average window temperature for different situations. The average values for the 3D numerical simulations were obtained for part of the window that is underneath the three active row of burners.

Table 4.2: Comparison of average window temperature between 3D models and 1D model.

Model	No cooling	COS	RBS	Combined
3D - Avg window temperature, $\overline{T_w}$ [°C]	926	830	732	683
1D - Avg window temperature, $\overline{T_w}$ [°C]	889	758	502	446

The results show similar values for the situation without cooling, with a difference of only 30°C. The numerical simulations for the cases with cooling register higher differences. The simulations with cooling inside RBS demonstrate a higher difference due to the already observed cooling inefficiency in 3D simulations. The step height for the 3D numerical simulations is higher than the one used for the development of the 1D model (50 and 15 mm for three- and one-dimensional, respectively). The same effect of combined cooling is verified for both models, a reduction of around 50°C when compared with the cooling applied only in RBS. The value of radiative energy absorbed by the window for the combined cooling is also similar (15/17.8 kW/m² for 3D/1D model, respectively).

The extraction of the fluid mixture inside RBS is also evaluated in the 1D model developed, according with the energy balance (see Section 3.3.1).

For the operating conditions under consideration (combined cooling), the extracted gas temperature predicted by the 1D model and the 3D model is approximately equal to 698°C and 803°C, respectively. The higher 3D model exhaust temperature is explained by the role of furnace walls: furnace walls are neglected in the 1D model but not in the 3D model. Furnace walls are responsible for transferring a net radiative power to the surrounding fluid by convection heat transfer. This combination of heat transfer mechanisms at the furnace walls in the 3D model leads to an increase of the gas temperature at the exhaust section of the RBS.

4.5 Chapter conclusions

The numerical simulations of the full curing furnace identified a high window temperature for the situation without cooling ($\overline{T_w} = 929^\circ\text{C}$). The system is studied with a cooling system above and underneath the glass window.

The cooling inside COS is in agreement with previous results for the convection heat transfer coefficient (Figure 3.21). The results of an analysis with cooling inside RBS show a negligible difference between different cooling schemes (A and C), which is in agreement with the the results of the previous chapter (see Section 3.2.8). The alignment of cooling scheme C inside RBS between burner's output

and cooling slot will lead to a reduced average window temperature. The analysis of the flow field inside RBS show that part of the wall jet does not attach in a correct way to the window due to the high step at the entrance ($h = 10b$). Cooling inside COS (underneath the window) has a lower effect than cooling inside RBS (above the window) as already proved in previous chapter.

The energy balances are verified and the radiative flux which reaches the coil is the necessary to drive the thermochemical process. The system can also be considered as adiabatic due to the wall constituent materials. However, the radiative gain of the walls match a convection loss to the fluid. This effect is not negligible and is not considered in the 1D model, justifying the differences observed between 1D and 3D model.

Chapter 5

Conclusions

The present work analyzes the processes inherent to curing furnace by IR radiative energy exchange, specifically, the thermal control of the window glass to guarantee the safety of the operation. The configuration of the system considered uses a glass plate partition inside the oven and registers high temperatures due its absorption of radiation. Window cooling in form of cold wall jets allows to remove heat from the medium.

Different turbulence models in wall jets were investigated numerically to perform a validation study of the numerical error associated to simulation of wall jets. Due to construction constraints, the cold wall jets face a backward step at the entrance and the numerical studies demonstrated that after the attachment almost at the edge of the plate, the flow behaves as a typical wall jet.

A 1D model of the window with discrete ordinates method was developed to predict and analyse the thermal behaviour of the glass. An increase of the thickness will result in a logarithmic increase of the absorption and consequently, window temperature.

Numerical simulations were performed to obtain the heat transfer correlations associated to the wall jet cooling for the specific cases studied. This information is integrated in the 1D model developed to an extensive analysis. The cooling system demonstrated a high impact on the reduction of the temperature. Cooling inside COS (underneath the glass) has a lower effect than cooling inside RBS (above the window) for the nominal operating condition. The effect is a result of the reduced mass flow rate and high cooling gas temperature defined at the injection of COS. The burner's output has a negligible effect on cooling inside RBS due to the reduced velocity ratio and the injection of a cold wall jet with a certain angle brings negligible differences.

Three different cooling strategies are analysed and compared. The 1D model developed is used not just in an average evaluation but in local regions to provide the temperature gradient. Cooling from two-sides leads to less heat removed from the window and higher gradient of temperature due to the stagnation region at the middle of the plate. There is no significant difference on the total heat removed from the window by considering cooling from one-side or in alternated scheme.

The optimization procedure leads to the optimal cooling conditions (minimum cooling power) for certain safety requirements (maximum window temperature and gradient of temperature). The demand

of cooling power increases when there is a need of a lower maximum temperature.

The numerical simulations of the full curing furnace demonstrated similar conclusions and results obtained with the 1D model developed. The results also identified the high window temperature for the situation without cooling (929°C). The results of an analysis with cooling inside RBS show a negligible difference between different cooling schemes (one-sided or alternated). The energy balances were verified and the system can be considered as adiabatic due to the wall constituent materials and dimensions. However, the radiative gain of the walls matches with a convection heat loss to the fluid. This effect is not negligible and is not considered in the 1D model, justifying the differences observed between the 1D and 3D models.

5.1 Achievements

A thermal control of the window is achieved by an extensive study during this work. The main conclusions from the work are then:

- $k-\omega$ SST and SA turbulence models with low-Re modeling have higher accuracy on the prediction of thermal and flow field in non-isothermal wall jets.
- The results and conclusions obtained with the 1D model developed were similar to the results of full 3D numerical simulations. The models predict high window temperatures for the case without cooling (889°C) and an high impact of cooling by wall jets.
- The optimization shows that the additional cooling on the lower section is a relevant contribution for energetic purposes and that there is not a universal best choice for the scheme of cooling because that depends on the safety requirements - an alternated cooling scheme is a more efficient choice but presents higher thermal gradients than cooling from one-side.

5.2 Future work

Further work can be developed considering unsteady effects and thermal stresses to the glass. In addition, round jets (different diameters and spacing [67]) instead of a continuous slot can be studied. Pulse jets (amplitude and frequency) can also be investigated. The effects of the lateral walls on the 1D window model will result in an increase of the complexity of the model but can result on an increase of the model accuracy.

References

- [1] L. Lori, A. Tamba, F. Deflorian, L. Fedrizzi, and P. L. Bonora. Stainless steel as new substrate for coil coating. *Progress in Organic Coatings*, 27(1-4):17–23, 1996. ISSN 03009440. doi: 10.1016/0300-9440(95)00528-5.
- [2] D. Santos, M. R. Costa, and M. T. Santos. Performance of polyester and modified polyester coil coatings exposed in different environments with high UV radiation. 58:296–302, 2007. doi: 10.1016/j.porgcoat.2007.01.006.
- [3] T. Kolås, A. Røyset, M. Grandcolas, and A. Lacau. Solar energy materials and solar cells cool coatings with high near infrared transmittance for coil coated aluminium. *Solar Energy Materials and Solar Cells*, 196(December 2018):94–104, 2019. ISSN 0927-0248. doi: 10.1016/j.solmat.2019.03.021.
- [4] Energy Efficient Coil Coating Process, European Project. URL <https://www.spire2030.eu/ecco>.
- [5] R. Viskanta and R. J. Grosh. Heat transfer by simultaneous conduction and radiation in an absorbing medium. *Journal of Heat Transfer*, 84(1):63–72, 1962.
- [6] P. Talukdar and S. C. Mishra. Analysis of conduction-radiation problem in absorbing, emitting and anisotropically scattering media using the collapsed dimension method. *International Journal of Heat and Mass Transfer*, 45(10):2159–2168, 2002. ISSN 00179310.
- [7] S. P. Marques, E. J. Barbero, and J. S. Murillo. Analysis of conduction-radiation problem in absorbing and emitting nongray materials. *International Journal of Numerical Methods for Heat and Fluid Flow*, 19(2):165–181, 2009.
- [8] S. Chandrasekhar. *Radiative transfer*. New York: Dover, 1960.
- [9] S. T. Thynell. Discrete-ordinates method in radiative heat transfer. *International Journal of Engineering Science*, 36(12-14):1651–1675, 1998.
- [10] G. Hu, C. M. Schietekat, Y. Zhang, F. Qian, G. Heynderickx, K. M. Van Geem, and G. B. Marin. Impact of radiation models in coupled simulations of steam cracking furnaces and reactors. *Industrial and Engineering Chemistry Research*, 54(9):2453–2465, 2015.

- [11] J.-J. Hwang and C.-S. Cheng. Impingement cooling in triangular ducts using an array of side-entry wall jets. *International Journal of Heat and Mass Transfer*, 44(5):1053–1063, 2001. ISSN 0017-9310. doi: [https://doi.org/10.1016/S0017-9310\(00\)00141-1](https://doi.org/10.1016/S0017-9310(00)00141-1).
- [12] M. B. Glauert. The wall jet. *Journal of Fluid Mechanics*, 1(06):625, 1956.
- [13] B. E. Launder and W. Rodi. The turbulent wall jet measurements and modeling. *Annual Review of Fluid Mechanics*, 15(1):429–459, 1983.
- [14] W. H. Schwarz and W. P. Cosart. The two-dimensional turbulent wall-jet. *Journal of Fluid Mechanics*, 10(04):481, 1961.
- [15] A. Verhoff. The two-dimensional, turbulent wall jet with and without external stream. *Department of Aeronautical Engineering, Princeton University, Princeton, NJ*, 1963.
- [16] W. K. George, H. Abrahamsson, J. Eriksson, R. I. Karlsson, L. Lofdahl, and M. Wosnik. A similarity theory for the turbulent plane wall jet without external stream. *Journal of Fluid Mechanics*, 425:367–411, 2000.
- [17] I. Wygnanski, Y. Katz, and E. Horev. On the applicability of various scaling laws to the turbulent wall jet. *Journal of Fluid Mechanics*, 234(-1):669, 1992.
- [18] H. Abrahamsson, B. Johansson, and L. Lofdahl. A turbulent plane two-dimensional wall-jet in a quiescent surrounding. *Eur. J. Mech. B/Fluids* 13, pages 533–556, 1994.
- [19] J. P. J. G. Eriksson, R. I. Karlsson. An experimental study of a plane turbulent wall jet using LDA. 25:50–60, 1998.
- [20] M. Mahmoudi, D. Nobes, and B. Fleck. An experiment design for measuring the velocity field of a round wall jet in counter-flow. *International Journal of Mechanical Engineering and Mechatronics*, 2014. doi: 10.11159/ijmem.2014.003.
- [21] T. Dakos, C. A. Verriopoulos, and M. M. Gibson. Turbulent flow with heat transfer in plane and curved wall jets. *Journal of Fluid Mechanics*, 145(-1):339, 1984.
- [22] R. S. AbdulNour, K. Willenborg, J. J. McGrath, J. F. Foss, and B. S. AbdulNour. Measurements of the convection heat transfer coefficient for a planar wall jet: Uniform temperature and uniform heat flux boundary conditions. *Experimental Thermal and Fluid Science*, 22(3-4):123–131, 2000.
- [23] I. Z. Naqavi, J. C. Tyacke, and P. G. Tucker. A numerical study of a plane wall jet with heat transfer. *International Journal of Heat and Fluid Flow*, 63:99–107, 2017.
- [24] J. C. Akfirat. Transfer of heat from an isothermal flat plate to a two-dimensional wall jet. In *Proceeding of International Heat Transfer Conference 3*, pages 274–279, Connecticut, 1966.
- [25] B. A. Kader and A. M. Yaglom. Heat and mass transfer laws for fully turbulent wall flows. *International Journal of Heat and Mass Transfer*, 15(12):2329–2351, 1972. ISSN 00179310.

- [26] J. R. Howell. *Thermal Radiation Heat Transfer*. CRC Press, 2010.
- [27] N. Karmarkar. A new polynomial-time algorithm for linear programming. *Combinatorica*, 4(4):373–395, 1984. ISSN 0209-9683. doi: 10.1007/BF02579150.
- [28] F. A. Potra and S. J. Wright. Interior-point methods. 124:281–302, 2000.
- [29] M. H. Wright. The interior-point revolution in optimization: history, recent developments, and lasting consequences. 42(1):39–56, 2004.
- [30] K. Ponnambalam, A. Vannelli, and T. E. Unny. An application of Karmarkar’s interior-point linear programming algorithm for multi-reservoir operations optimization. *Stochastic Hydrology and Hydraulics*, 3(1):17–29, 1989. ISSN 0931-1955. doi: 10.1007/BF01543425.
- [31] V. H. Quintana, S. M. leee, G. L. Torres, S. Member, J. Medina-palomo, and M. leee. Interior-point methods and their applications to power systems : A classification of publications and software Codes. 8950(l):170–176, 2000.
- [32] F. Glover. A template for scatter search and path relinking. In J.-K. Hao, E. Lutton, E. Ronald, M. Schoenauer, and D. Snyers, editors, *Artificial Evolution*, pages 1–51, Berlin, Heidelberg, 1998. Springer Berlin Heidelberg. ISBN 978-3-540-69698-8.
- [33] Z. Ugray, L. Lasdon, J. Plummer, F. Glover, J. Kelly, and R. Martí. Scatter search and local NLP solvers: A multistart framework for global optimization. *INFORMS Journal on Computing*, 19(3):328–340, 2007. ISSN 1091-9856. doi: 10.1287/ijoc.1060.0175.
- [34] J. H. Holland. *Adaptation in natural and artificial systems: An introductory analysis with applications to biology, control and artificial intelligence*. MIT Press, Cambridge, MA, USA, 1992. ISBN 0262082136.
- [35] Yeniay. Penalty function methods for constrained optimization with genetic algorithms. *Mathematical and Computational Applications*, 10(1):45–56, 2005. ISSN 2297-8747. doi: 10.3390/mca10010045.
- [36] A. Chehouri, R. Younes, J. Perron, and A. Ilinca. A constraint-handling technique for genetic algorithms using a violation factor. *Journal of Computer Science*, 12(7):350–362, 2016. doi: 10.3844/jcssp.2016.350.362.
- [37] B. Launder and D. Spalding. The numerical computation of turbulent flows. *Computer Methods in Applied Mechanics and Engineering*, 3(2):269–289, 1974. ISSN 0045-7825.
- [38] W. Jones and B. Launder. The prediction of laminarization with a two-equation model of turbulence. *International Journal of Heat and Mass Transfer*, 15(2):301–314, 1972. ISSN 0017-9310. doi: [https://doi.org/10.1016/0017-9310\(72\)90076-2](https://doi.org/10.1016/0017-9310(72)90076-2).
- [39] T.-H. Shih, W. W. Liou, A. Shabbir, Z. Yang, and J. Zhu. A new k- eddy viscosity model for high reynolds number turbulent flows. *Computers Fluids*, 24(3):227–238, 1995. ISSN 0045-7930.

- [40] S.-E. Kim, D. Choudhury, and M. V. Otugen. A near-wall treatment using wall functions sensitized to pressure gradient, symposium; fluids engineering and laser anemometry conference, separated and complex flows. In *Separated and complex flows, ASME -PUBLICATIONS- FED, Symposium; Fluids engineering and laser anemometry conference, Separated and complex flows*, volume 217, pages 273–280. ASME;, 1995. ISBN 0791814726.
- [41] Z. Yang and T. H. Shih. New time scale based k-epsilon model for near-wall turbulence. *AIAA J.*, 31:1191–1198, 1992.
- [42] K. Abe, T. Kondoh, and Y. Nagano. A new turbulence model for predicting fluid flow and heat transfer in separating and reattaching flows-i. flow field calculations. *International Journal of Heat and Mass Transfer*, 37(1):139–151, 1994. ISSN 0017-9310. doi: 10.1016/0017-9310(94)90168-6.
- [43] F. R. Menter. Two-equation eddy-viscosity turbulence models for engineering applications. *AIAA journal*, 32(8):1598–1605, 1994.
- [44] P. R. Spalart and S. R. Allmaras. A one-equation turbulence model for aerodynamic flows. In *AIAA Paper 1992-0439*, page 1, 1992.
- [45] F. B. Hsiao and S. S. Sheu. Experimental studies on flow transition of a plane wall jet. *Aeronautical Journal*, 100(999):373–380, 1996.
- [46] A. Pattamatta and G. Singh. Assessment of turbulence models in the prediction of flow field and thermal characteristics of wall jet. *Frontiers in Heat and Mass Transfer*, 3, 2012. doi: 10.5098/hmt.v3.2.3005.
- [47] A. Neale, D. Derome, B. Blocken, and J. Carmeliet. CFD calculation of convective heat transfer coefficients and validation - part 2: Turbulent flow. 2021.
- [48] E. Pulat and E. Beyazoglu. Computational investigation of confined wall inclination effects on impinging jet fluid flow and heat transfer. *International Journal of Thermal Sciences*, 163:106749, 2021. ISSN 1290-0729. doi: <https://doi.org/10.1016/j.ijthermalsci.2020.106749>.
- [49] T. D. Nguyen and H. Souad. PIV measurements in a turbulent wall jet over a backward-facing step in a three-dimensional, non-confined channel. *Flow Measurement and Instrumentation*, 42:26–39, 2015.
- [50] N. Nait Bouda, R. Schiestel, M. Amielh, C. Rey, and T. Benabid. Experimental approach and numerical prediction of a turbulent wall jet over a backward facing step. *International Journal of Heat and Fluid Flow*, 29(4):927–944, 2008.
- [51] N. D. Eryou and L. R. Glicksman. An experimental and analytical study of radiative and conductive heat transfer in molten glass. *Journal of Heat Transfer*, 94(2):224–230, 1972.
- [52] D. M. Planck. *The Theory of Heat Radiation*. P. Blakiston's Son & Co, 1914.

- [53] T. L. Bergman, A. S. Lavine, F. P. Incropera, and D. P. DeWitt. *Fundamentals of Heat and Mass Transfer*. John Wiley & Sons, 8th edition, 2017.
- [54] D. F. Swinehart. The Beer-lambert law. *Journal of Chemical Education*, 39(7):333, 1962. doi: 10.1021/ed039p333.
- [55] R. Hui and M. O'Sullivan. Chapter 1 - fundamentals of optical devices. In R. Hui and M. O'Sullivan, editors, *Fiber Optic Measurement Techniques*, pages 1–128. Academic Press, Boston, 2009. ISBN 978-0-12-373865-3. doi: <https://doi.org/10.1016/B978-0-12-373865-3.00001-X>.
- [56] N. Zuckerman and N. Lior. Jet impingement heat transfer: Physics, correlations, and numerical modeling. *Advances in Heat Transfer*, 39(C):565–631, 2006.
- [57] H. Martin. Heat and mass transfer between impinging gas jets and solid surfaces. *Advances in Heat Transfer*, 13(C):1–60, 1977.
- [58] W. Sutherland. The viscosity of gases and molecular force. *The London, Edinburgh, and Dublin Philosophical Magazine and Journal of Science*, 36(223):507–531, 1893. doi: 10.1080/14786449308620508.
- [59] M. W. Chase. *NIST-JANAF Thermochemical Tables*. American Institute of Physics, 1998.
- [60] ANSYS Fluent Theory Guide. ANSYS Fluent Theory Guide. *ANSYS Inc., USA*, 15317(November): 724–746, 2013.
- [61] M. Rubin. Optical properties of soda lime silica glasses. *Solar Energy Materials*, 12(4):275–288, 1985.
- [62] R. J. Kind and K. Suthanthiran. The interaction of two opposing plane turbulent wall jets. *Journal of Fluid Mechanics*, 58(2):389–402, 1973. doi: 10.1017/S002211207300265X.
- [63] P. S. Johansson and H. I. Anderson. Direct numerical simulation of two opposing wall jets. *Physics of Fluids*, 17(5):1–11, 2005. ISSN 10706631. doi: 10.1063/1.1920627.
- [64] S. Arabia. A numerical study of the flow and heat- transfer characteristics of an impinging laminar slot-jet including crossflow effects. 35:2501–2513, 1992.
- [65] J. M. M. Barata and D. F. G. Dura. Laser-Doppler measurements of impinging jet flows through a crossflow. 36(1):665–674, 2004. doi: 10.1007/s00348-003-0737-3.
- [66] B. Sunde and H. Abrahamsson. Heat transfer characteristics of an impinging jet in crossflow. (2011), 2014. doi: 10.1115/1.4004527.
- [67] S. C. Godi, A. Pattamatta, and C. Balaji. Heat transfer from a single and row of three dimensional wall jets - a combined experimental and numerical study. *International Journal of Heat and Mass Transfer*, 159:119801, 2020. ISSN 0017-9310. doi: <https://doi.org/10.1016/j.ijheatmasstransfer.2020.119801>.

